Research article

Progressive axonopathy when oligodendrocytes lack the myelin protein CMTM5

Tobias J. Buscham[1], Maria A. Eichel-Vogel[1], Anna M. Steyer[1,2], Olaf Jahn[3,4], Nicola Strenzke[5], Rakshit Dardawal[6], Tor R. Memhave[6], Sophie B. Siems[1], Christina Müller[7], Martin Meschkat[1,8], Ting Sun[1], Torben Ruhwedel [1,2], Wiebke Möbius[1,2], Eva-Maria Krämer-Albers[7], Susann Boretius[6], Klaus-Armin Nave[1] and Hauke B. Werner[1,*]

Affiliations

[1]Department of Neurogenetics, Max Planck Institute of Experimental Medicine, 37075 Göttingen, Germany
[2]Electron Microscopy Core Unit, Max Planck Institute of Experimental Medicine, 37075 Göttingen, Germany
[3]Proteomics Group, Max Planck Institute of Experimental Medicine, 37075 Göttingen, Germany
[4]Translational Neuroproteomics Group, Department of Psychiatry and Psychotherapy, University Medical Center Göttingen, Georg-August-University, 37075 Göttingen, Germany
[5]Institute for Auditory Neuroscience, University Medicine Göttingen, 37075 Göttingen, Germany
[6]Functional Imaging Laboratory, German Primate Center, Leibniz Institute for Primate Research 37077 Göttingen, Germany
[7]Institute of Developmental Biology and Neurobiology, Johannes Gutenberg University, 55128 Mainz, Germany
[8]Abberior Instruments Gmbh, 37077 Göttingen, Germany

***Corresponding author**
Dr. Hauke Werner
Max Planck Institute of Experimental Medicine
Department of Neurogenetics
Hermann-Rein-Str. 3; D-37075 Göttingen, Germany
Tel.: +49 (551) 3899-759
E-Mail: Hauke@em.mpg.de

Keywords
Oligodendrocyte; myelin sheath; axon-glia interaction; axon degeneration; neuropathology; focused ion beam-scanning electron microscopy (FIB-SEM); differential myelin proteome analysis

Reviewer login information to the proteome data repository:
Project: Progressive axonopathy when oligodendrocytes lack the myelin protein CMTM5
Project accession: PXD029443
Reviewer account: Username: reviewer_pxd029443@ebi.ac.uk; Password: 2nTEI47v

Word and figure count
3548 words (main text); 7 main figures; 6 supplemental figures, 2 tables

Abstract

Oligodendrocytes facilitate rapid impulse propagation along the axons they myelinate and support their long-term integrity. However, the functional relevance of many myelin proteins has remained unknown. Here we find that expression of the tetraspan-transmembrane protein CMTM5 (Chemokine-like factor-like MARVEL-transmembrane domain containing protein 5) is highly enriched in oligodendrocytes and CNS myelin. Genetic disruption of the *Cmtm5*-gene in oligodendrocytes of mice does not impair the development or ultrastructure of CNS myelin. However, oligodendroglial *Cmtm5*-deficiency causes an early-onset progressive axonopathy, which we also observe in global and in tamoxifen-induced oligodendroglial *Cmtm5*-mutants. Presence of the *Wld*^{s} mutation ameliorates the axonopathy, implying a Wallerian degeneration-like pathomechanism. These results indicate that CMTM5 is involved in the function of oligodendrocytes to maintain axonal integrity rather than myelin biogenesis.

Introduction

Myelination of axons by oligodendrocytes enables rapid, saltatory conduction of signals in the vertebrate central nervous system (CNS) (Cohen et al., 2020; Hartline & Colman, 2007; Tasaki, 1939). Additionally, oligodendrocytes support the long-term preservation of axons metabolically (Fünfschilling et al., 2012; Lee et al., 2012; Philips et al., 2021; Saab et al., 2016) and via extracellular vesicles (Chamberlain et al., 2021; Frühbeis et al., 2020; Mukherjee et al., 2020). In fact, myelin pathology in CNS disorders such as leukodystrophies, multiple sclerosis and respective animal models is commonly associated with axonal degeneration (Franklin et al., 2012; Stadelmann et al., 2019; Wolf et al., 2021). Oligodendrocytes are thus required to maintain axonal integrity and ultimately CNS function. However, oligodendrocytes express thousands of transcripts (Jäkel et al., 2019; Zhang et al., 2014; Zhou et al., 2020) and myelin comprises hundreds of proteins (Ishii et al., 2009; Jahn et al., 2020), and our knowledge remains limited with respect to which molecules contribute to myelin biogenesis, axonal support, or both.

We recently found that a member of the chemokine-like factor-like MARVEL-transmembrane containing (CMTM) protein family, CMTM6, is expressed in Schwann cells, the myelinating cells of the peripheral nervous system (PNS), and that its deletion in mice affects the diameters and function of peripheral axons (Eichel et al., 2020). Based on this finding we asked if a member of the CMTM family is expressed in oligodendrocytes, which may thus fulfill a similar function in the CNS. The CMTM protein family comprises eight members in humans (Han et al., 2003) that have mostly been associated with mediating tumor immunity (Burr et al., 2017; Mezzadra et al., 2017; Shao et al., 2007; Xiao et al., 2015; Yuan et al., 2020).

In this study we focused on *Cmtm5* considering (i) its expression in oligodendrocytes according to bulk RNAseq data (Zhang et al., 2014), (ii) the finding that the *Cmtm5* gene promoter drives expression of Cre recombinase in oligodendrocytes (Gong et al., 2007), and (iii) the mass spectrometric identification of CMTM5 in CNS myelin (Jahn et al., 2020). By structure prediction, CMTM5 comprises four transmembrane domains with small intracellular N- and C-terminal domains and two small extracellular loops (Jumper et al., 2021) but, its name notwithstanding, no apparent chemokine-like sequence motif. Here we assess the functional relevance of CMTM5 in oligodendrocytes. We find that CMTM5 is not required for normal myelination or axonal diameters in the CNS. However, our data indicate that CMTM5 is involved in the function of oligodendrocytes to maintain the integrity of CNS axons.

Results

Expression of CMTM5 is enriched in oligodendrocytes and CNS myelin

We explored the hypothesis that CNS myelin comprises a homolog of the recently identified (Eichel et al., 2020) PNS myelin protein CMTM6. Indeed, previous mass spectrometric analysis identified CMTM5 (Chemokine-like factor-like MARVEL-transmembrane domain-containing family member-5) in myelin purified from the brains of C57/Bl6 mice (Jahn et al., 2020). In contrast, neither CMTM6 nor any other member of the protein family was detected in CNS myelin. Correspondingly, published RNA sequencing data (Zhang et al., 2014) demonstrate that mature oligodendrocytes (MOL) display substantial abundance of *Cmtm5* mRNA but not of any other gene family member (**Figure 1–Supplement 1A**). Indeed, *Cmtm5* mRNA is enriched in the oligodendrocyte lineage, in which its abundance increases with differentiation from the progenitor (OPC) stage to the MOL stage (**Figure 1–Supplement 1B**). When evaluating mRNA abundance according to published scRNA-seq data (Jäkel et al., 2019; Zhou et al., 2020), MOL (as annotated by high-level expression of myelin basic protein mRNA, *MBP/Mbp*) express *CMTM5*/*Cmtm5* mRNA in both humans and mice (**Figure 1–Supplement 1C-F**).

To independently confirm CMTM5 as a myelin protein, we first used immunoblotting to assess its abundance in myelin biochemically purified from mouse brains in comparison to equal amounts of mouse brain lysate. One band was detected at the expected molecular weight of 18 kDa. Indeed, the abundance of CMTM5 was markedly higher in the myelin-enriched fraction than in brain lysates (**Figure 1A**), similar to the myelin markers PLP, CNP and SIRT2. Confocal imaging of immunolabeled spinal cord sections revealed CMTM5 in CNS myelin of c57Bl/6N mice (**Figure 1B**). Importantly, no labeling was found when analyzing corresponding sections of newly generated conditional mouse mutants with a deletion of the *Cmtm5* gene in in myelinating cells ($Cmtm5^{fl/fl}$*$Cnp^{Cre/WT}$, also termed cKO; see below) (**Figure 1B**). By immunoblotting of homogenized wild-type mouse brains, the abundance of CMTM5 increased coinciding with myelin formation and maturation between postnatal days 15 (P15) and P24 (**Figure 1C**). In adult mouse brains between 6 and 24 months (m) of age, the abundance of CMTM5 remained unchanged (**Figure 1C**). The abundance of CMTM5 in purified myelin also remained essentially constant (**Figure 1D**). Taken together, expression of CMTM5 in the CNS is largely limited to oligodendrocytes and enriched in CNS myelin.

CMTM5 is not essential for myelin biogenesis and composition

To assess the functional relevance of the expression of *Cmtm5* by oligodendrocytes, we generated mouse mutants with a conditional deletion of the gene selectively in myelinating

cells (*Cmtm5*$^{fl/fl}$**Cnp*$^{Cre/WT}$, also termed cKO). Conditional mutants were born at expected frequencies, and cKO mice showed no obvious behavioral phenotype. We biochemically purified myelin from brains of cKO mice and respective controls at P75 and further examined if CMTM5-deficiency affects the protein composition of myelin. By immunoblotting, CMTM5 was readily detected in myelin purified from the brains of control mice but undetectable in *Cmtm5* cKO myelin (**Figure 2A**). By label-free quantitative proteome analysis, *Cmtm5* cKO mice displayed a largely similar myelin proteome composition as control mice (**Figure 2B,B´**). As an exception, CMTM5 was undetectable in myelin purified from the brains of *Cmtm5* cKO mice, and the relative abundance of CNP was approximately halved as previously shown for the utilized *Cnp*$^{Cre/WT}$ driver mice owing to heterozygosity of the *Cnp* gene (Erwig, et al., 2019; Lappe-Siefke et al., 2003).

To examine if loss of CMTM5 affects the biogenesis and ultrastructure of myelin, we used transmission electron microscopy to assess optic nerves dissected from cKO and control mice at P30 and P75 (**Figure 2C-L**). By morphometry, we did not observe signs of hypomyelination (**Figure 2D,I**) or myelin pathology such as myelin outfoldings, inner tongue swellings or lamella splittings (**Figure 2E,J**). The thickness of myelin sheaths, as determined by the g-ratio, was also virtually the same in cKO and control mice (**Figure 2F-G, K-L**). By immunohistochemistry, *Cmtm5* cKO mice displayed an unaltered number of cells immunopositive for carbonic anhydrase 2 (CAII), a marker for mature oligodendrocytes (**Figure 2M,N**). We then used magnetic resonance imaging (MRI) to assess the brains of 8-months old *Cmtm5* cKO and respective control mice. However, no apparent differences in brain morphometry and diffusivity were found in various white and gray matter areas (**Figure 2-Supplement 1**). Together, these data imply that expression of CMTM5 by oligodendrocytes is not essential for the normal biogenesis, ultrastructure or protein composition of CNS myelin.

Cmtm5 **deletion in oligodendrocytes causes early-onset progressive axonopathy and late-onset general neuropathology**

Considering that the diameters of peripheral axons are increased when Schwann cells lack CMTM6 (Eichel et al., 2020), we asked whether the diameters of CNS axons are altered when oligodendrocytes lack CMTM5. Yet, the quantitative assessment of transmission electron micrographs did not reveal abnormal axonal diameters in the optic nerves of cKO mice (**Figure 3-Supplement 1A,B**). Axonal diameters were also normal in mice lacking CMTM5 in all cells (*Cmtm5*$^{-/-}$) compared to respective controls (**Figure 3-Supplement 1C**).

However, in the course of this analysis we noted a considerable number of pathological-appearing axonal profiles. When quantifying these profiles at three different ages, we found

their frequency to increase over time in the optic nerves of *Cmtm5* cKO compared to control mice (**Figure 3A,B**). Pathological profiles were evident in *Cmtm5* cKO optic nerves already at P30, and their number progressively increased toward 1 year of age, the oldest analyzed timepoint. We observed a trend toward a reduced number of axons in *Cmtm5* cKO mice at P30 and P75 that reached significance at 1 year of age (**Figure 3C**). This implies that the observed axonal pathology ultimately leads to axonal loss. To test whether *Cmtm5* cKO mice display pathological profiles also in other white matter tracts, we used electron microscopy to assess the dorsal white matter in spinal cords at 1 year of age. Indeed, the number of pathological profiles was increased several-fold in *Cmtm5* cKO compared to control mice (**Figure 3D,E**), indicating that the observed axonopathy is not restricted to the optic nerve.

We then used magnetic resonance spectroscopy (MRS) to determine the concentrations of the metabolites myo-Inositol and N-Acetyl-Aspartate (NAA), which are considered neuropathological markers reflecting gliosis and axonal degeneration respectively. We found the concentrations of myo-Inositol significantly increased in the corpus callosi of *Cmtm5* cKO compared to control mice at 8 months of age (**Figure 3-Supplement 2A**). *Cmtm5* cKO brains displayed a trend toward reduced concentrations of NAA, which did not reach significance (**Figure 3-Supplement 2B**). We considered that these findings may imply the emergence of general neuropathology in the CNS of *Cmtm5* cKO mice, which we then aimed to resolve temporally. To this aim we subjected the brains of *Cmtm5* cKO mice to immunohistochemistry at the ages of P30, P75 and 1 year. We immunolabeled axonal swellings (using antibodies against APP), astrocytes (using antibodies against GFAP) and microglia (using the markers IBA1/AIF1 and MAC3/LAMP2). For quantification, we selected the hippocampal fimbria as a relatively uniform white matter tract. At age P30 and P75 we found no genotype-dependent differences between *Cmtm5* cKO and control mice with respect to number of APP-immunopositive axonal swellings or the relative area of immunopositivity for GFAP, IBA1 or MAC3. At one year of age, however, all markers were significantly increased in *Cmtm5* cKO compared to control mice (**Figure 3-Supplement 3I-L**).

Pathology of axon/myelin units by focused ion beam-scanning electron microscopy

Considering that 2-dimensional visualization allows only limited insight into morphological features, we next assessed pathological profiles in the optic nerves of one year old *Cmtm5* cKO mice using 3-dimensional reconstruction of datasets gained by focused ion beam-scanning electron microscopy (**Figure 4**). We found that the numbers of myelin outfoldings, inner-tongue inclusions, and axoplasmic inclusions are not increased in *Cmtm5* cKO mice (**Figure 4A´´-C´´**). Interestingly, however, the number of myelin whorls are markedly increased in *Cmtm5* cKO mice (**Figure 4D´´**). Myelin whorls are multilamellar structures that largely

display the periodicity of CNS myelin devoid of a discernible axon, probably best interpreted as remnants of degenerating myelinated fibers with relative sparing of myelin membranes (Edgar et al., 2009). These data indicate that axonal degeneration - but not myelin pathology such as myelin outfoldings or inner-tongue inclusions – emerges when oligodendrocytes lack CMTM5.

Functional assessment of retinae and optic nerves

As a read-out for visual function, we first assessed retinal function by electroretinography (ERG) recordings from *Cmtm5* cKO and control mice at 34 weeks of age. ERG waveforms (**Figure 5A**), ERG thresholds (**Figure 5B**) and the amplitudes of the a- and b-waves (**Figure 5C,D**) did not differ between the genotypes, indicating normal retinal function. However, visually evoked potentials (VEPs) implied that transmission of signals via the optic nerves to the visual cortex was impaired in *Cmtm5* cKO mice (**Figure 5E-H**). All mice displayed sizeable VEPs (**Figure 5E**) with normal thresholds (**Figure 5F**) and a normal VEP latency (**Figure 5G**), indicating normal speed of action potential propagation and probably reflecting normal myelination in the optic nerves. However, the VEP amplitudes were significantly reduced in *Cmtm5* cKO mice (**Figure 5H**), probably owing to the axonopathy (**Figure 3, 4**).

Axonopathy in constitutive and tamoxifen-induced *Cmtm5*-mutants

All results presented thus far are based on the analysis of mice in which the *Cmtm5* allele was recombined by Cre expressed in myelinating cells under control of the *Cnp* promoter. Importantly, the utilized heterozygous $Cnp^{Cre/Wt}$ driver mice (Lappe-Siefke et al., 2003) harbor only one functional *Cnp* allele. Notwithstanding that heterozygous $Cnp^{Cre/Wt}$ mice display neuropathology only at old age (Hagemeyer et al., 2012), we sought to test if *Cmtm5* mutant mice also display axonopathy on a homozygous wild-type *Cnp* gene background. To this aim we bred mice carrying a homozygous deletion of the *Cmtm5* gene in all cells ($Cmtm5^{-/-}$, Knock-out; $Cmtm5^{wt/wt}$, Control). As expected, CMTM5 was readily detectable by immunoblot in myelin purified from the brains of control mice but undetectable in $Cmtm5^{-/-}$ myelin. Importantly, the abundance of CNP appeared similar in $Cmtm5^{-/-}$ and $Cmtm5^{wt/wt}$ control myelin (**Figure 6A**), as was that of the myelin marker SIRT2. *Vice versa*, the abundance of CMTM5 appeared similar by immunoblot analysis of purified from the brains of $Plp^{-/Y}$ and $Cnp^{-/-}$ and respective control mice (**Figure 6-Supplement 1A,B**). Thus, the abundance of PLP and CNP in myelin does not depend on CMTM5 and *vice versa* the abundance of CMTM5 in myelin does not depend on PLP or CNP.

We then used conventional transmission electron microscopy to scrutinize optic nerves dissected from $Cmtm5^{-/-}$ mice. Notably, by quantitative assessment of electron micrographs

we found a progressive increase in the number of pathological profiles in *Cmtm5*$^{-/-}$ compared to control mice (**Figure 6B,C**), in similarity to *Cmtm5* cKO mice (**Figure 3**). Importantly, this indicates that the axonopathy that emerges when oligodendrocytes lack CMTM5 is independent of *Cnp* heterozygosity.

To rule out that the pathological profiles in *Cmtm5* mutant mice are the consequence of subtle developmental defects, we used the *Plp*^{CreERT2} driver line (Leone et al., 2003) to induce recombination of the *Cmtm5* gene by injecting tamoxifen into adult *Cmtm5*$^{fl/fl}$**Plp*^{CreERT2} mice (termed *Cmtm5* iKO in the following). Tamoxifen injected *Cmtm5*$^{fl/fl}$ mice served as controls. By immunoblot, the abundance of CMTM5 was greatly reduced in myelin purified from the brains of *Cmtm5* iKO mice four months after tamoxifen injection (4 mo PTI) (**Figure 6D**). Importantly, by quantitative assessment of electron micrographs, *Cmtm5* iKO mice displayed a significantly increased number of pathological profiles 4 mo PTI (**Figure 6E, F**). This indicates that continued oligodendroglial expression of CMTM5 in adult mice is required to prevent the emergence of axonopathy.

Axonopathy upon *Cmtm5* deletion is counteracted by the Wallerian degeneration slow (*Wld*^{s}) mutation

To test if the axonopathy in *Cmtm5* mutants causes a decline in the number of neuronal cell bodies, we quantified retinal ganglion cells (RGC) in the retinae of *Cmtm5* cKO and control mice at 1 year of age (**Figure 7A-C**). We found that RGC numbers were similar, indicating that neuronal cell bodies are preserved. Considering that this finding may imply a Wallerian-type pathomechanism of axon degeneration (Coleman & Höke, 2020) we assessed if the presence of the *Wld*^{s} mutation (Coleman et al., 1998; Lunn et al., 1989) affects the number of pathological profiles upon *Cmtm5* deficiency. Indeed, when we analyzed the optic nerves of *Cmtm5*$^{-/-}$ mice by transmission electron microscopy (TEM) at the age of 6 months, presence of the *Wld*^{s} mutation markedly reduced the number of pathological profiles (**Figure 7D-E**). For comparison *Cmtm5*$^{wt/wt}$ mice displayed only a negligible number of pathological profiles, independent of the presence of the *Wld*^{s} mutation. Together, these results imply a Wallerian-type pathomechanism of axonopathy when oligodendrocytes lack *Cmtm5*.

Discussion

We report the intriguing observation that mice lacking the CNS myelin protein CMTM5 display an early-onset progressive axonopathy, whereas the biogenesis and ultrastructure of myelin appear unaffected. According to previously established datasets, expression of *Cmtm5* in the CNS is highly enriched in myelinating oligodendrocytes (Jäkel et al., 2019; Zhang et al., 2014; Zhou et al., 2020). CMTM5 is not the first myelin protein associated with secondary axonal degeneration in mutant mice. However, different from the previously studied myelin genes *Plp1* (Edgar et al., 2004; Griffiths I et al., 1998; Lüders et al., 2019) and *Cnp* (Edgar et al., 2009; Lappe-Siefke et al., 2003), the encoded protein is of much lower abundance in the myelin sheath. By quantitative mass spectrometry, CMTM5 represents only 0.027% of the myelin proteome (Jahn et al., 2020), in comparison to 37.9% for PLP and 5.1% for CNP. The relative abundance of CMTM5 in myelin is thus roughly equivalent to that of other transmembrane-tetraspan proteins CD9 (0.06%), proteolipid GPM6B (0.04%) and the gap junction protein GJC3/Cx29 (0.02%) (Jahn et al., 2020), which were previously identified as low-abundant myelin constituents (Kagawa et al., 1997; Kleopa et al., 2004; Werner et al., 2013). Considering the low abundance of CMTM5 in myelin, it may not be unexpected that CMTM5-deficient mice do not display primary ultrastructural defects that affect the myelin sheath when highly abundant structural myelin proteins as PLP or CNP are lacking (**Table 1**). The comparison of our different mouse mutants has revealed that CMTM5 is required by mature oligodendrocytes. However, details of its mechanistic role in continued axon-glia interactions remain obscure.

CMTM5 is a member of the chemokine-like factor-like MARVEL-transmembrane containing (CMTM) protein family (Han et al., 2003) that has been associated with regulating tumor immunity (Burr et al., 2017; Mezzadra et al., 2017; Shao et al., 2007; Xiao et al., 2015; Yuan et al., 2020), including CMTM5 itself. Comparatively little is known about the functional relevance of CMTM proteins in the nervous system. However, we recently found the paralog CMTM6 to be expressed in myelinating Schwann cells, in which it is involved in the previously unknown function of Schwann cells to restrict the diameters of peripheral axons (Eichel et al., 2020). The consequences of deleting CMTM5 and CMTM6 in oligodendrocytes and Schwann cells, respectively, may appear roughly similar when considering that the myelin ultrastructure is not affected while axonal features are altered. Notably, however, deleting CMTM6 from Schwann cells causes increased diameters of peripheral axons but no signs of actual degeneration (Eichel et al., 2020) whereas deleting CMTM5 from oligodendrocytes causes CNS axonopathy without altering axonal calibers. Thus, CMTM5 and CMTM6 expressed by oligodendrocytes and Schwann cells have distinct functions in the CNS and the PNS, respectively.

The axonopathy observed upon deleting *Cmtm5* strongly implies that CMTM5 is involved in the oligodendroglial function of preserving axonal integrity and that this function is not limited to an early developmental stage. Oligodendroglial support of axons involves several mechanisms, including supplying energy-rich substrates via monocarboxylate transporters (Fünfschilling et al., 2012; Lee et al., 2012; Philips et al., 2021; Trevisiol et al., 2020), allocating antioxidative proteins and other enzymes via extracellular vesicles (Chamberlain et al., 2021; Frühbeis et al., 2020; Mukherjee et al., 2020), and modulating axonal transport (Edgar et al., 2004; Frühbeis et al., 2020), these mechanisms being possibly interrelated. It will be an important next step to identify the specific mechanism(s) of axonal support that are impaired when oligodendrocytes lack CMTM5.

It is helpful to compare the pathology of previously described myelin mutants with the axonal defects in CMTM5-deficient mice as assessed here. Notably, the presence of early-onset, progressive axonopathy is a shared feature of the myelin mutant mice lacking PLP (Edgar et al., 2004; Griffiths et al., 1998), CNP (Edgar et al., 2009; Lappe-Siefke et al., 2003) or CMTM5, which are normally myelinated (*Cmtm5*-mutants) or display only moderate hypomyelination (*Plp1* and *Cnp*-mutants). In contrast, entirely dysmyelinated *Mbp*-deficient *shiverer* mice (Roach et al., 1985) do not display axonal degeneration (Griffiths I et al., 1998; Ou et al., 2009; Uschkureit et al., 2000). This indicates that the lack of myelin *per se* is less detrimental for axons than axonal ensheathment with functionally impaired myelin. Moreover, APP-immunopositive axonal swellings, astrogliosis and microgliosis are early features when PLP (Griffiths et al., 1998; de Monasterio-Schrader et al., 2013; Edgar et al., 2004; Steyer et al., 2020; Trevisiol et al., 2020) or CNP (Edgar et al., 2009; Lappe-Siefke et al., 2003; Wieser et al., 2013) are lacking, but emerges at much older age in CMTM5-deficient mice. This indicates that the pathomechanisms differ between *Plp1* and *Cnp*-mutants and *Cmtm5*-mutants. This is supported by our observation that the axonopathy is ameliorated by the presence of the *Wld*^{S} mutation in CMTM5-deficient mice, different form that in PLP- and CNP-deficient mice, at least at the examined time points and in presence of one copy of the *Wld*^{S} gene (Edgar et al., 2004, 2009). Together, this implies different dynamics, and probably different mechanisms of axonopathy when oligodendrocytes lack PLP, CNP or CMTM5.

The *Wlds* mutation can protect axons from various types of physical, toxic or genetic insult (Coleman et al., 1998; Coleman & Höke, 2020; Lunn et al., 1989). In the *Wld*^{S} pathway, a key regulator of axonal degeneration is the enzyme sterile alpha and TIR motif containing protein 1 (SARM1) (Gerdts et al., 2013; Osterloh et al., 2012). Both, the *Wld*^{S} mutation and deletion of the *Sarm1* gene can delay axonal degeneration (Coleman et al., 1998; Hopkins et al., 2021),

354 involving the maintenance of high NAD^+ levels along the axon (di Stefano et al., 2015; Gilley
355 & Coleman, 2010; Hopkins et al., 2021; Wang et al., 2005).To the best of our knowledge,
356 CMTM5-deficient mice represent the first model in which the axonopathy that emerges upon
357 deletion of a CNS myelin protein is ameliorated by the *Wld*^{S} mutation. Only the degeneration
358 of axons in the PNS of mice lacking myelin protein zero (MPZ/P0) is robustly delayed by the
359 presence of the *Wld*^{S} mutation (Samsam et al., 2003). Thus, genetic defects of
360 oligodendrocytes or Schwann cells can cause an axonopathy with a Wallerian-like
361 pathomechanism in the CNS and PNS, respectively. It will be important to test if the currently
362 developed small molecule SARM1 inhibitors (Bosanac et al., 2021; Hughes et al., 2021; Loring
363 et al., 2020) allow counteracting axonal degeneration secondary to an insult primarily affecting
364 oligodendrocytes.
365
366

Material and Methods

Mouse models and mouse lines

Frozen sperm of mice carrying the 'knockout-first' allele of the *Cmtm5* gene (C57BL/6N-A^{tm1Brd} *Cmtm5*$^{tm1a(KOMP)Wtsi}$*/Wtsi*) was acquired from The Mouse Genetics Project (Wellcome Trust Sanger Institute, Hinxton, UK). *Cmtm5*$^{tm1a(KOMP)Wtsi}$ mice were generated by the transgene facility of the Max Planck Institute of Experimental Medicine (Göttingen, Germany) by *in vitro* fertilization using standard procedures. The LacZ/neo cassette was deleted by crossbreeding these mice with *Gt(ROSA)26Sor*$^{tm1(FLP1)Dym}$ mice expressing flippase (Farley et al., 2000) yielding mice heterozygous for the floxed *Cmtm5* allele (*Cmtm5*$^{tm1c(KOMP)Wtsi}$ mice, also termed *Cmtm5*$^{fl/+}$) which were bred to homozygosity. To delete *Cmtm5* in oligodendrocytes, *Cmtm5*$^{fl/fl}$ mice were crossbred with mice expressing *Cre* under the *Cnp* promoter (*Cnp1*$^{tm(cre\ puro)Kan}$ mice, also termed *Cnp*$^{Cre/WT}$; Lappe-Siefke et al., 2003) yielding *Cmtm5*$^{fl/fl}$**Cnp*$^{Cre/WT}$ mice (also termed *Cmtm5* cKO). In experiments assessing *Cmtm5* cKO mice, *Cmtm5*$^{fl/fl}$ mice served as controls. Taking advantage of germline-recombination we gained a mouse line with a body-wide deletion of *Cmtm5* (*Cmtm5*$^{tm1d(KOMP)Wtsi}$ mice, also termed *Cmtm5*$^{-/-}$ or Knock-out). In experiments assessing *Cmtm5*$^{-/-}$ mice, *Cmtm5*$^{+/+}$ mice served as controls. To delete *Cmtm5* in oligodendrocytes of adult mice, *Cmtm5*$^{fl/fl}$ were crossbred with mice expressing tamoxifen-inducible *Cre* under the *Plp* promoter (Tg(Plp1-cre/ERT2)1Ueli, *Plp*^{CreERT2},Leone et al., 2003) resulting in *Cmtm5*$^{fl/f*}$ *Plp*^{CreERT2} mice (also termed *Cmtm5* iKO) and respective controls without *Cre.* For induction, male mutant mice (*Cmtm5*$^{fl/f*}$ *Plp*^{CreERT2}) and male control mice (*Cmtm5*$^{fl/fl}$) were injected with Tamoxifen intraperitoneally at 8 weeks of age for 10 days with a 2-day break after the first five injection days (1 mg tamoxifen dissolved in 100 µl corn oil per mouse and day). *Cmtm5*$^{+/-}$ mice were crossbred with *Cmtm5*$^{+/-}$ mice harboring the *WLD*^{S} mutation (Wld^{s}, Coleman et al., 1998; Mack et al., 2001) to obtain all experimental groups from the same breeding scheme (Control groups: *Cmtm5*$^{+/+}$ and *Cmtm5*$^{+/+}$**Wld*^{s}; knock-out groups: *Cmtm5*$^{-/-}$ and *Cmtm5*$^{-/-}$**Wld*^{s}). Littermate mice were used as experimental controls as far as possible.

Genotyping was carried out by genomic PCR. *Cmtm5* genotypes were assessed with the same PCR strategy in all *Cmtm5* lines (*Cmtm5* cKO, *Cmtm5*$^{-/-}$, *Cmtm5* iKO, *Cmtm5*Wld*^{s}). Sense primer (5`-AGTAGTGGCC CATTGCCATC) in combination with antisense primer (5`-TGGTTAGGGG GCTCCTCTTC) yielded a 626 bp product (floxed allele) or 437 bp product (wildtype). In the same reaction, antisense primer (5`-GAGCTCAGAC CATAACTTCG) was used to detect *Cmtm5* allele recombination yielding a 313 bp fragment. Detection of the *Cnp*^{Cre} allele (Lappe-Siefke et al., 2003) was carried out using sense primer (5'-GCCTTCAAAC TGTCCATCTC) and antisense primer (5'-CCCAGCCCTT TTATTACCAC) amplifying a 700 bp product. As well as a sense (5'-CAGGGTGTTA TAAGCAATCCC) and antisense (5'-

CCTGGAAAAT GCTTCTGTCCG) primer yielding a 357bp fragment when Cre positive. *Plp*^{CreERT2} (Leone et al., 2003)was detected using sense primer (5`-TGGACAGCTG GGACAAAGTAAGC) and antisense primer (5`-CGTTGCATCG ACCGGTAATGCAGGC) yielding a 250 bp product. The *Wlds* mutation (Coleman et al., 1998; Mack et al., 2001) was detected using sense primer (5`-CGTTGGCTCT AAGGACAGCAC) and antisense primer (5`-CTGCAGCCCC CACCCCTT) yielding a 182 bp product.

Mice were bred and kept in the mouse facility of the Max Planck Institute of Experimental Medicine, Göttingen. Experimental mutant mice were analyzed with littermate controls as far as possible. All animal experiments were performed in accordance with the German animal protection law (TierSchG) and approved by the Niedersächsisches Landesamt für Verbraucherschutz und Lebensmittelsicherheit (LAVES) under license 33.19-42502-04-15/1833 and 33.8-42502-04-19/3172.

Biochemical purification of myelin from mouse brains

Purification of a myelin-enriched light weight membrane fraction from nervous tissue using sucrose density centrifugation and osmotic shocks was previously described (Erwig, Patzig, et al., 2019). Mice were sacrificed by cervical dislocation. Protein concentrations of brain lysate and myelin fractions were determined using the DC Protein Assay Kit (Bio-Rad, Munich, Germany) following the manufacturer´s instruction and measured using the Eon™ High Performance Microplate Spectrophotometer (BioTek, Vermont, USA).

Immunoblotting

Immunoblotting was essentially performed as described (Schardt et al., 2009). Brain lysate and myelin fraction samples were diluted in 4x SDS sample buffer (Glycerol 40% [w/v], Tris/HCl pH 6.8 240mM, sodium dodecyl sulfate (SDS) 8% [w/v] Bromphenol blue 0.04% [w/v]; 5% Dithiothreitol (DTT) was added as a reducing agent. Before usage, samples were heated at 40°C for 10 min. For protein separation by SDS-PAGE, the Mini-PROTEAN Handcast system (BioRad, Munich, Germany) was used with self-casted acrylamide gels (10-15%). 5-15 µg samples were loaded per well (depending on protein of interest) next to 5 µl pre-stained protein ladder (PageRuler™, ThermoFischer Scientific, Waltham, USA). Proteins were separated by constant current (200V) for 45-60 min using a BioRad power supply. Immunoblotting was carried out with a Novex® Semi-Dry Blotter (Invitrogen, Karlsruhe, Germany) and proteins were transferred to an activated (100% Ethanol, 1 min; followed by two washing steps with water) PVDF membrane (GE Healthcare, Buckinghamshire, UK; Cat# 10600023) at 20V for 45 min. After blotting, membranes were blocked in 1xTBS containing 5% non-fat dry milk (Frema, Karlsruhe, Germany) and 0.05% Tween-20 for one hour at room temperature (RT).

Primary antibodies were diluted in 5 ml blocking buffer and incubated overnight at 4°C and horizontal rotation. Membranes were washed thrice with TBS-T for 5-10 min each and incubated for one hour with secondary HRP antibodies diluted in blocking buffer. Membranes were washed three times with TBS-T for 5-10 min. Detection was carried out using enhanced chemiluminescent detection (ECL) according to the manufacturer´s instructions (Western Lightning® Plus-ECL or SUperSignal™ West Femto Maximum Sensitive Substrate; Thermo Fischer Scientific, St Leon-Rot, Germany). Immunoblots were scanned using ECL Chemostar (Intas Science Imaging, Göttingen, Germany). For antibody information see **Table 2**.

Label-free quantification of myelin proteins

In-solution digestion of myelin proteins according to an automated filter-aided sample preparation (FASP) protocol (Patzig et al., 2016) and LC-MS-analysis by different MS^E-type data-independent acquisition (DIA) mass spectrometry approaches was performed as recently established for PNS (Siems et al., 2020) and CNS (Jahn et al., 2020) myelin. Briefly, protein fractions corresponding to 10 µg myelin protein were dissolved in lysis buffer (1% ASB-14, 7 M urea, 2 M thiourea, 10 mM DTT, 0.1 M Tris pH 8.5) and processed according to a CHAPS-based FASP protocol in centrifugal filter units (30 kDa MWCO, Merck Millipore). After removal of the detergents, protein alkylation with iodoacetamide, and buffer exchange to digestion buffer (50 mM ammonium bicarbonate (ABC), 10 % acetonitrile), proteins were digested overnight at 37°C with 400 ng trypsin. Tryptic peptides were recovered by centrifugation and extracted with 40 µl of 50 mM ABC and 40 µl of 1% trifluoroacetic acid (TFA), respectively. Combined flow-throughs were directly subjected to LC-MS-analysis. For quantification according to the TOP3 approach (Silva et al., 2006), aliquots were spiked with 10 fmol/µl of Hi3 EColi standard (Waters Corporation), containing a set of quantified synthetic peptides derived from E. coli. Chaperone protein ClpB.

Nanoscale reversed-phase UPLC separation of tryptic peptides was performed with a nanoAcquity UPLC system equipped with a Symmetry C18 5 µm, 180 µm × 20 mm trap column and a HSS T3 C18 1.8 µm, 75 µm × 250 mm analytical column (Waters Corporation) maintained at 45°C. Peptides were separated over 120 min at a flow rate of 300 nl/min with a gradient comprising two linear steps of 3-35% mobile phase B (acetonitrile containing 0.1% formic acid) in 105 min and 35-60% mobile phase B in 15 min, respectively. Mass spectrometric analysis on a quadrupole time-of-flight mass spectrometer with ion mobility option (Synapt G2-S, Waters Corporation) was performed in the dynamic range-enhanced (DRE)-$UDMS^E$ mode as established previously for proteome analysis of purified myelin (Jahn et al., 2020; Siems et al., 2020). Continuum LC-MS data were processed using Waters ProteinLynx Global Server (PLGS) and searched against a custom database compiled by

adding the sequence information for E. coli. Chaperone protein ClpB and porcine trypsin to the UniProtKB/Swiss-Prot mouse proteome (release 2017-07, 16909 entries) and by appending the reversed sequence of each entry to enable the determination of false discovery rate (FDR). Precursor and fragment ion mass tolerances were automatically determined by PLGS and were typically below 5 ppm for precursor ions and below 10 ppm (root mean square) for fragment ions. Carbamidomethylation of cysteine was specified as fixed and oxidation of methionine as variable modification. One missed trypsin cleavage was allowed. Minimal ion matching requirements were two fragments per peptide, five fragments per protein, and one peptide per protein. The FDR for protein identification was set to 1% threshold.

For post-identification analysis including TOP3 quantification of proteins, ISOQuant (Distler et al., 2014; Kuharev et al., 2015) software freely available at www.isoquant.net) was used as described previously (Jahn et al., 2020; Siems et al., 2020). Only proteins represented by at least two peptides (minimum length six amino acids, score ≥ 5.5, identified in at least two runs) were quantified as parts per million (ppm), i.e. the relative amount (w/w) of each protein in respect to the sum over all detected proteins. FDR for both peptides and proteins was set to 1% threshold and at least one unique peptide was required. Proteome profiling comparing myelin from *Cmtm5* cKO and CTRL mice was performed with three biological replicates and duplicate digestion, resulting in a total of 6 LC-MS runs per condition. The mass spectrometry proteomics data have been deposited to the ProteomeXchange Consortium via the PRIDE (Perez-Riverol et al., 2019) partner repository with dataset identifier **PXD029443**.

Electron microscopy

For transmission electron microscopy (TEM) optic nerves and spinal cords were dissected and fixed in Karlsson-Schulz fixative (4% PFA, 2.5% Glutaraldehyde in 0.1 M phosphate buffer) overnight. Samples were processed and embedded in epoxy resin (Serva, Heidelberg, Germany) as described (Möbius et al., 2010). For TEM, ultrathin (50 nm) sections were prepared using a PTPC Powertome Ultramicrotome (RMC, Tuscon Arizona, USA) and a diamond knife (Diatome AG, Biel, Switzerland). Sections were cut and collected on formwar coated copper grids (AGAR scientific, Essex, UK). To enhance contrast, ultrathin sections were stained with UranyLess (Electron Microscopy Science, Hatfield, Panama) for 20 min and washed 6 times with $_{dd}H_20$. For analysis 16-20 non-overlapping random images were taken per animal using the Zeiss EM900 at 7000x (one image = 220 µm^2). All image analysis was performed using Fiji (Version 2.0.0-rc-68/1.52i; Schindelin et al., 2012).

To assess relative number of pathological axons (degenerated axons, axonal swellings) and pathological myelin (myelin outfoldings, double myelination, inner tongue swelings) units, all

axons on 16-20 non-overlapping random images were analyzed per mouse. For axon diameter analysis, all normal-appearing, accurately cross-sectioned myelinated axons were evaluated on 16-20 non-overlapping random images. Data is presented as mean axonal diameter per animal. g-ratios were calculated as ratio between axonal diameter and the outer diameter of the corresponding myelin sheath. In total 180-200 axons were randomly selected for g-ratio analysis from 16-20 EM images per mouse using the Fiji Grid tool (Circular grids, 3 μm^2 per point, random offset).

For the analysis of axon number, semithin sections (thickness 500 nm) were cut and stained with methylene blue/azur II (1:1) for one minute followed by a washing step with H_2O. Images were acquired at 100x using a bright-field light microscope (Zeiss AxioImager Z1 coupled to a Zeiss Axio Cam MRc camera; controlled and stitched by Zeiss Zen 1.0 software). Using Fiji, optic nerve images were separated into 55 μm^2 rectangles. From all rectangles filled with ON tissue 5 were chosen at random and all axons were counted. Axon number is shown as mean of 5 assessed rectangles per mouse.

Focused ion beam – scanning electron microscopy

Samples were prepared according to (Steyer et al., 2020). In brief, dissected optic nerve samples were immersed in primary fixative (Karlsson-Schultz phosphate buffer: 109.5 mM $NaH_2PO_4 \cdot H_2O$, 93.75 mM $Na_2HPO_4 \cdot 2H_2O$, 86.2 mM NaCl, 2.5% glutaraldehyde, 4% formaldehyde. Adjust the pH to 7.4 and filter, at 4 °C for at least 24 h) and processed with a modified OTO-protocol (osmium-thiocarbohydrazide-osmium) as previously described (Weil et al., 2018) based on a previously established original protocol (Deerinck et al., 2010). Briefly, samples were post-fixed for 3 h with 2% OsO_4 (EMS, Hatfield, USA) and 1.5% $K_3Fe(CN)_6$ (EMS, Hatfield, USA) at 4°C followed by a contrasting step with 1% thiocarbohydrazide (Sigma-Aldrich, St. Louis, USA) for 1 h at room temperature and 1.5 h incubation with 2% OsO_4. *En bloc* staining was performed with 2% uranyl acetate overnight at 4°C. The next day the samples were dehydrated through a series of ascending concentrations of acetone (EMS, Hatfield, USA) for 15 min each (30%, 50%, 75%, 90%, 3× 100%) and incubated with increasing concentrations of the epoxy resin Durcupan (Sigma-Aldrich, St. Louis, USA) (2:1, 1:1, 1:2) for 2 h each and left over night in 90% Durcupan without component D. The next day the samples were incubated with 100% Durcupan (all components: A (epoxy resin) 11.4 g, B (hardener) 10 g, C (accelerator) 0.3 g, D (plasticizer) 0.1 g) for 4.5 h and polymerized for 48 h at 60°C.

The polymerized samples were trimmed using a 90° trimming knife (Diatome AG, Biel, Switzerland) and positioned on a SEM-stub using silver conductive resin (EPO-TEK 129-4) (EMS, Hatfield, USA). The surface was sputter coated (Leica, ACE 600) (Leica, Wetzlar,

552 Germany) with a layer of 10 nm platinum and placed inside the FIB-SEM (Crossbeam 540,
553 Zeiss, Oberkochen, Germany). After exposing a cross-section through the region of interest
554 with 15 nA ion current and polishing with 7 nA, a 400 nm deposition of platinum was performed
555 using 3 nA. The final dataset was acquired at 1.5 kV (1000 pA) 5 nm × 5 nm × 25 nm voxel
556 size with a milling current of 1.5 nA. Fiji (Schindelin et al., 2012) was used for all following
557 image processing steps: The images were aligned using the SIFT algorithm, cropped and
558 inverted. They were smoothed using a Gaussian blur (sigma 1) and a local contrast
559 enhancement was applied (CLAHE: blocksize 127, histogram bins 256, maximum slope 1.25).
560 The dataset was binned by 2 in x and y. Analysis of pathological myelin and axon profiles was
561 carried out using Fiji. All profiles in the volume belonging to one of the categories (myelin
562 outfoldings, inner-tongue inclusions, axoplasmic inclusions, myelin whorls) were counted, and
563 values were normalized to a volume of 10000 μm^3. Example 3D models were reconstructed
564 using IMOD (v 4.9.12, University of Colorado, https://bio3d.colorado.edu/imod).
565
566 **Immunohistochemistry**
567 Sections (5 µm) of paraffin-embedded brains were used to determine neuropathology and
568 oligodendrocyte number. Section preparation was as previously described (de Monasterio-
569 Schrader et al., 2012; Patzig et al., 2016). To assess neuropathology in *Cmtm5* cKO and
570 control mice, 3-5 mice per genotype were analyzed for each timepoint (P30, P75, P365) and
571 labelled for amyloid precursor protein (APP) (Chemicon, 1:1000), MAC3 (Pharmingen, 1:400),
572 glial fibrillary acidic protein (GFAP) (Novo Castra, 1:200) or IBA1 (abcam, 1:1000). Images
573 were acquired at 40x magnification using a bright-field light microscope (Zeiss AxioImager Z1,
574 coupled to Zeiss AxioCam MRc Camera; controlled and stitched by Zeiss Zen 1.0 software).
575 The hippocampal fimbria was analyzed by counting APP positive axonal swellings per selected
576 area or by using an ImageJ plugin to semiautomatically determine the area of
577 GFAP/MAC3/IBA1 immunopositivity as previously described (de Monasterio-Schrader et al.,
578 2012; Lüders et al., 2017; Patzig et al., 2016). To assess oligodendrocyte number, sections of
579 paraffin-embedded brains from *Cmtm5* cKO and control mice at P75 were deparaffinized and
580 rehydrated as with sections for neuropathology. Sections were then blocked for 1 hour at room
581 temperature with PBS containing BSA and horse serum. Incubation with primary antibody was
582 then carried out over 48h at 4°C with anti-CAII antibody (1:300 in PBS containig 1% HS). Slides
583 were washed thrice for 10 minutes with PBS and incubated with DAPI (Thermo Scientific,
584 Waltham, USA) and anti-rabbit Alexa555 (Dianova, 1:1000 in PBS containing 1% HS). Slides
585 were washed again thrice with PBS for 10 minutes and mounted using AquaPolymount. The
586 hippocampal fimbria was imaged using the Axio Observer Z2 (Zeiss) at a 40x magnification
587 and stitched using Zeiss Zen2011. All cells positive for both DAPI and CAII were identified as

oligodendrocytes. All positive cells were counted and normalized to an area of 1 mm^2. For antibody information see **Table 2**.

Preparation of cryosections and confocal imaging

Cryosection were obtained from spinal cords immersion fixed with 4% PFA overnight. Nerves were then transferred to a sucrose buffer (10% [w/v], 20% [w/v], 30% [w/v] in 0.1 M phosphate buffer) over night at 4°C for each concentration. The nerves were then embedded in small plastic chambers using Tissue-Tek® O.C.T.™ Compound (Sakura, Staufen, Germany). Nerves were stored at -20°C until further use. 10 µm thick cross-sections were prepared using a cryostat (Reichert Jung® Cryocut 18000, Wetzlar, Germany) and transferred to Superfrost® Plus microscope slides (Thermo Fischer Scientific, St. Leon-Rot, Germany). Slides were dried for 30 minutes at room temperature and stored at -20°C until further use.

Sections were stained with the following protocol using 200 µl volumes per slide: 3 minutes Methanol, 30 minutes permeabilization using PBS with 0.4% [v/v] Triton-X100 (Sigma Aldrich, St. Louis, USA) followed by blocking using DAKO blocking buffer (DAKO, Hamburg, Germany) for 60 minutes. TUJ1 (Covance) and CMTM5 (custom made by Pineda, Berlin, Germany Table 2) antibodies were diluted in antibody diluent (DAKO, Hamburg, Germany) and incubated for 48 hours at 4°C in a dark, humid chamber. Sections were then washed three times with PBS for 10 minutes and incubated with secondary antibodies (α-rabbit STAR-RED, α-mouse STAR-ORANGE, abberior, Göttingen, Germany, Table 2) diluted 1:200 in antibody diluent for 60 minutes. Sections were washed 3 times with PBS for 10 minutes and mounted using AquaPolymount (Polysciences, Warrington, USA). Images were obtained on a Confocal and STED FACILITY line microscope (Abberior Instruments, Germany) and acquired as xy-plane with a pixel size of 30nm. The fluorophores were excited with appropriate excitation lasers at 640nm (abberior STAR RED) and 561nm (abberior STAR ORANGE). For image acquisition the microscope software “Lightbox” as provided by Abberior Instruments was used.

Magnetic Resonance Imaging and Spectroscopy

Magnetic resonance imaging (MRI) and spectroscopy (MRS) were acquired on a 9.4T Bruker BioSpec MR system with a 30 cm horizontal bore and B-GA12 gradient system operating on Bruker ParaVision 6.0.1 (Hardware and software from Bruker BioSpin MRI GmbH, Ettlingen, Germany). A four-channel (2×2) receive-only mouse head coil was used, in combination with a 112/84 resonator, to acquire MRI and MRS (both from Bruker BioSpin MRI GmbH, Ettlingen).

The MRI protocol included magnetization transfer (MT)-weighted images and diffusion-weighted images. For MT, a 3D fast low angle shot (FLASH) sequence was used to acquire

three datasets: MT-weighted, proton density-weighted, and T1-weighted (repetition time [15.1, 15.1, 18] ms, echo time 3.4 ms, flip angles [5˚, 5˚, 25˚], two averages, voxel size 100 µm × 100 µm × 100 µm, acquisition time 18.4 min). These datasets were used to estimate MT saturation (MTsat) according to the method described by (Helms et al., 2008). Diffusion-weighted images (DWI) were acquired using a spin-echo echo-planar imaging sequence (repetition time 2000 ms, echo time 21.5 ms, two repetitions, voxel size 100 µm × 100 µm × 500 µm, gradient duration and separation 2.5 ms and 12.5 ms, b values 0, 1000 and 2000, gradient directions 30 for each b value, acquisition time 17.2 min). These DWI were preprocessed through denoising (Fadnavis et al., 2020) and averaged across repetitions. A diffusion tensor model (Basser et al., 1994) was fitted to the preprocessed DWI data, and fractional anisotropy (FA), axial diffusivity (AD), radial diffusivity (RD), and mean diffusivity (MD) maps were derived (Garyfallidis et al., 2014). Multi-echo gradient-recalled echo (GRE) images were acquired using a 3D GRE sequence (repetition time 25 ms, echo time 2.2 ms, echo spacing 2 ms, number of echoes 10, flip angle 12˚, four averages, voxel size 70 µm × 70 µm × 300 µm, acquisition time 19 min). The effective transverse relaxation rate (R_2^*) maps were calculated using by fitting the multi-echo GRE magnitude signal decay across all echo times with a mono-exponential model (Pei et al., 2015).

MRS was acquired from cortices and corpus callosi using a stimulated echo acquisition mode (STEAM) sequence. The parameters of the STEAM sequence were: repetition time of 6000 ms, echo time of 10 ms, spectral width of 5000 Hz, 2048 data points, 128 averages, and a total acquisition time of 12:48 min. The dimensions of the cortical and corpus callosal voxels were 3.9×0.7×3.2 mm^3 and 3.9×0.7×1.7 mm^3, respectively. All spectra were acquired with CHESS water suppression and outer volume suppression. The spectra were analyzed and quantified using LCModel (Provencher, 1993) in the chemical shift range from 0.2 to 4.2 ppm. Values with Cramer-Rao lower bounds above 20% were excluded from further analyses. Statistics were performed in *Excel* using a 2-tailed, unpaired Student´s t-test assuming equal variance.

Electroretinography (ERG) and visually evoked potentials (VEP)

ERGs were recorded as described (Dieck et al., 2012) and VEP were recorded essentially as described (Ridder & Nusinowitz, 2006). Briefly, mice were dark adapted overnight and anesthetized with Ketamin (125µg/g), Xylazin (2,5µg/g) and Buprenorphin i.p. (0,1 mg/kg). Eyes were kept moist using contact lens solution containing hyaluronic acid for ERG recordings and with Methocel (DuPont Pharma, Mississauga, Canada) for VEP recordings. For ERG recordings, a silver ball electrode placed in the outer angle of the left eye served as active electrode. Signals were averaged 10 times. For VEP recordings, the scalp was resected and a small hole was drilled on the right side 1 mm lateral and 1mm rostral of lambda and a thin

needle electrode was inserted superficially. Signals were averaged at least 50 times. The reference electrode was placed on the nose of the mouse and the common ground near the hind legs. Signals were amplified 1000 times (NeuroAmp) and sampled without analog filtering. 0.1 ms light flashes were generated using BioSig Software and TDT system III hardware (Tucker Davis Technologies, Davis, USA) and presented via a custom-designed Ganzfeld apparatus at a stimulus rate of 0.5 Hz. Illumination was calibrated using a luxmeter (Mavolux 5032c, Nürnberg, Germany) and an Integrated Photodiode Amplifier 10530 (Integrated Photomatrix Limited, Dorchester, UK). Analysis was performed using custom written matlab scripts (version 2019b). For analysis of ERG and VEP thresholds, Student´s t-test was applied. Data from ERG and VEP analysis (**Figure 5**) is represented in line graphs showing mean values of mice per genotype ±SEM. To determine the genotype-dependent effect on ERG and VEP amplitude and latencies across various light intensities, 2-way-ANOVA was applied.

Retina preparation and assessment of retinal ganglion cell number

To assess retinal ganglion cell numbers (RGC), eyes of 1 year old *Cmtm5*$^{-/-}$ mice and respective controls were dissected and fixed for one hour with 4% PFA/Phosphate Buffer (PB). Eyes were then rinsed in PB and retinae were dissected as follows. The eye was cut open along the ciliary body and cornea and lens were removed. The retinal pigment epithelium (RPG) was carefully removed. Four cuts on opposing sites were made to flatten the retina. The retina was transferred into a 24 well plate with 1 retina per well containing PBS. Retinae were washed with PBS/2% Triton X-100 (500 µl/well) at room temperature and gentle agitation for 10 minutes. To permeate nuclear membranes the wash solution was replaced by fresh PBS/2% Triton X-100 and retinae were frozen at -80°C for 10 minutes. Retinae were washed twice with PBS/0.5% Triton X-100 for 5 minutes at room temperature. To reduce unspecific AB binding retinae were incubated with blocking buffer (PBS/ 5%BSA/ 5% Donkey Serum/ 2% Triton X-100) for 1 hour at room temperature with gently agitation. To label RGCs, retinae were incubated with guinea pig anti-RBPMS (Sigma-Aldrich, St. Louis, USA); 1:200 in blocking buffer, 350 µl per well) for 2 hours at room temperature. Retinae were then washed thrice with PBS/0.5% Triton X-100 for 10 minutes at RT. RGCs were labelled using donkey anti-guinea pig Alexa 555 (1:1000 in blocking buffer) and incubated over night at 4°C. Retinae were then washed thrice for 30 minutes with PBS and transferred to a superfrost slide with a fine brush. Retinae were mounted using AquaPolymount with the RGC layer facing up. Slides were kept at 4°C and dark until imaging. Images were taken using the Axio Observer Z2 (Zeiss) and a 40x magnification and stitched using Zeiss Zen2011. For assessment of RGC number the average of 3 different areas (area= mm^2 per rectangle) were analyzed for each part of the retina (inner/middle/outer). Retinae of three individual mice per genotype were analyzed.

699 **Statistics**

700 All experiments were analyzed blinded to genotypes. Statistical assessment was performed
701 using GraphPad Prism 8 (GraphPad Software Inc., San Diego, United States) unless noted
702 otherwise. Two-sided Student´s t-test was used to compare two groups unless specified
703 otherwise. Welch´s correction was performed in case of unequal distribution. Levels of
704 significance were set as $p<0.05$ (*), $p<0.01$ (**) and $p< 0.001$ (***). Exact p-values are given in
705 the figure legends, except those for the MRI data in **Figure 2 Supplement 1** are listed below.
706 For all experiments, statistical test used and correction are given in the figure legend. Data in
707 **Figure 1 Supplement 1**; **Figure 2 D-E, I-J, N**; **Figure 3 B, C, E**; **Figure 3 Supplement 1**;
708 **Figure 3 Supplement 2**; **Figure 3 Supplement 3**, **Figure 4 A``-D``**; **Figure 6 C, F**; **Figure 7**
709 **C, E**; are given as bar graphs with mean ±SEM; data points represent individual mice. Data
710 from MRI analysis (**Figure 2 Supplement 1**) and ERG and VEP thresholds (**Figure 5 B, F**)
711 are presented as boxplots; data points represent individual mice. Data for frequency
712 distribution of axonal diameters (**Figure 3-Supplement 1 A´-C´**) are presented as bar graphs
713 showing binned axonal diameters pooled of all mice per condition. Proteome data (**Figure 2**
714 **B,B´**) is presented as volcano plot and heat map. Data correspond to 3 mice per genotype and
715 2 technical replicate per mouse. The Bioconductor R packages 'limma' and 'q-value' were used
716 to detect significant changes in protein abundance by moderated t-statistics as described
717 (Ambrozkiewicz et al., 2018; Siems et al., 2020). Further information is provided in **Figure 2B**
718 **source data 1**. g-ratios (**Figure 2 G, L**) are presented as scatter plots. Each data point
719 represents an individual axon. In total, 200 axons were analyzed per mouse and 5 mice were
720 analyzed per genotype. Data from ERG and VEP analysis (**Figure 5**) is represented in line
721 graphs showing mean values of mice per genotype ±SEM. To determine the genotype-
722 dependent effect on ERG and VEP amplitude and latencies across light intensities, 2-way-
723 ANOVA was applied.
724
725 Exact sample size and number of mice are given in the figures or in the figure legends, except
726 for the significance levels for MRI data in **Figure 2 supplement 1** which were as follows. CC,
727 Corpus callosum; Fim, Fimbria; Thal, Thalamus; Cort, Cortex; AC, Anterior commissure. Two-
728 sided Student´s t-test was applied. **(B)** CC: p= 0.1739; Fim: p= 0.2244; Thal: p= 0.3229; Cort:
729 p= 0.6159; AC: p= 0.3290. **(C)** CC: p= 0.7263; Fim: p= 0.2223; Thal: p= 0.9943; Cort: p=
730 0.5009; AC: p= 0.2425. **(D)** CC: p= 0.7103; Fim: p= 0.2608; Thal: p= 0.6903; Cort: p= 0.3576;
731 AC: p= 0.2531. **(E)** CC: p= 0.4374; Fim: p= 0.2038; Thal: p= 0.8343; Cort: p= 0.5728; AC: p=
732 0.2678. **(F)** CC: p= 0.7065; Fim: p= 0.8432; Thal: p= 0.7319; Cort: p= 0.8614; AC: p= 0.9983.
733

Data availability statement

The mass spectrometry proteomics data have been deposited to the ProteomeXchange Consortium via the PRIDE partner repository with dataset identifier **PXD029443**.

Ethics Statement

All animal experiments were performed in accordance with the German animal protection law (TierSchG). Ethical review of animal experiments was performed by the Niedersächsisches Landesamt für Verbraucherschutz und Lebensmittelsicherheit (LAVES) and approved with licenses 33.19-42502-04-15/1833 and 33.8-42502-04-19/3172.

Competing interest statement

MM is affiliated with Abberior Instruments Gmbh; the author has no financial interests to declare. KAN is a Reviewing Editor for eLIFE. All other authors declare no competing interest.

Funding

Deutsche Forschungsgemeinschaft (DFG) WE 2720/2-2 to HBW
Deutsche Forschungsgemeinschaft (DFG) WE 2720/4-1 to HBW
Deutsche Forschungsgemeinschaft (DFG) WE 2720/5-1 to HBW
European Research Council (ERC) Advanced Grant MyeliNano to KAN
The funders had no role in study design, data collection and interpretation, or the decision to submit the work for publication.

Acknowledgments

We thank S. Bode, K. Kötz, A. Fahrenholz, K. Fuhrmann, D. Hesse, R. Jung, U. Kutzke and S. Thom for technical assistance, G. Hoch for hardware development and technical support, U. Fünfschilling for *in vitro* fertilization, J. Groh for providing protocols, S. Ghandour and K. Kusch for antibodies, and J. Edgar for discussions. We thank the Wellcome Trust Sanger Institute Mouse Genetics Project (Sanger MGP) and its funders for providing the mutant mouse line *Cmtm5*$^{tm1a(KOMP)Wtsi}$.

Authors ORCIDs

Tobias J Buscham	http://orcid.org/0000-0002-6916-3102
Maria A Eichel-Vogel	http://orcid.org/0000-0002-9925-7249
Anna M. Steyer	http://orcid.org/0000-0002-4814-7517
Olaf Jahn	http://orcid.org/0000-0002-3397-8924
Nicola Strenzke	http://orcid.org/0000-0003-1673-1046
Rakshit Dadarwal	http://orcid.org/0000-0003-3091-2580
Tor R Memhave	http://orcid.org/0000-0002-3448-1581
Sophie B. Siems	http://orcid.org/0000-0002-7760-2507
Ting Sun	http://orcid.org/0000-0002-7104-7215
Torben Ruhwedel	http://orcid.org/0000-0002-9535-9395
Wiebke Möbius	http://orcid.org/0000-0002-2902-7165
Eva-Maria Krämer Albers	http://orcid.org/0000-0001-7994-1185
Susann Boretius	http://orcid.org/0000-0003-2792-7423
Klaus-Armin Nave	http://orcid.org/0000-0001-8724-9666
Hauke B Werner	http://orcid.org/0000-0002-7710-5738

References

Ambrozkiewicz, M. C., Schwark, M., Kishimoto-Suga, M., Borisova, E., Hori, K., Salazar-Lázaro, A., Rusanova, A., Altas, B., Piepkorn, L., Bessa, P., Schaub, T., Zhang, X., Rabe, T., Ripamonti, S., Rosário, M., Akiyama, H., Jahn, O., Kobayashi, T., Hoshino, M., … Kawabe, H. (2018). Polarity Acquisition in Cortical Neurons Is Driven by Synergistic Action of Sox9-Regulated Wwp1 and Wwp2 E3 Ubiquitin Ligases and Intronic miR-140. *Neuron*, *100*(5), 1097-1115.e15. https://doi.org/10.1016/j.neuron.2018.10.008

Basser, P. J., Mattiello, J., & Lebihan, D. (1994). MR Diffusion Tensor Spectroscopy and Imaging. *Biophysical Journal*, *66*, 259–267.

Bosanac, T., Hughes, R. O., Engber, T., Devraj, R., Brearley, A., Danker, K., Young, K., Kopatz, J., Hermann, M., Berthemy, A., Boyce, S., Bentley, J., & Krauss, R. (2021). Pharmacological SARM1 inhibition protects axon structure and function in paclitaxel-induced peripheral neuropathy. *Brain*. https://doi.org/10.1093/brain/awab184/6272578

Burr, M. L., Sparbier, C. E., Chan, Y. C., Williamson, J. C., Woods, K., Beavis, P. A., Lam, E. Y. N., Henderson, M. A., Bell, C. C., Stolzenburg, S., Gilan, O., Bloor, S., Noori, T., Morgens, D. W., Bassik, M. C., Neeson, P. J., Behren, A., Darcy, P. K., Dawson, S. J., … Dawson, M. A. (2017). CMTM6 maintains the expression of PD-L1 and regulates anti-Tumour immunity. *Nature*, *549*(7670), 101–105. https://doi.org/10.1038/nature23643

Chamberlain, K. A., Huang, N., Xie, Y., LiCausi, F., Li, S., Li, Y., & Sheng, Z.-H. (2021). Oligodendrocytes enhance axonal energy metabolism by deacetylation of mitochondrial proteins through transcellular delivery of SIRT2. *Neuron*, *109*(21), 3456–3472. https://doi.org/10.1016/j.neuron.2021.08.011

Cohen, C. C. H., Popovic, M. A., Klooster, J., Weil, M. T., Möbius, W., Nave, K. A., & Kole, M. H. P. (2020). Saltatory Conduction along Myelinated Axons Involves a Periaxonal Nanocircuit. *Cell*, *180*(2), 311–322. https://doi.org/10.1016/j.cell.2019.11.039

Coleman, M. P., Conforti, L., Anne Buckmaster, E., Tarlton, A., Ewing, R. M., Brown, M. C., Lyon, M. F., & Perry, V. H. (1998). An 85-kb tandem triplication in the slow Wallerian degeneration (Wld s) mouse. *Proceedings of the National Academy of Sciences*, *95*, 9985–9990. https://doi.org/10.1073/pnas.95.17.9985

Coleman, M. P., & Höke, A. (2020). Programmed axon degeneration: from mouse to mechanism to medicine. *Nature Reviews Neuroscience*, *21*(4), 183–196. https://doi.org/10.1038/s41583-020-0269-3

de Monasterio-Schrader, P., Jahn, O., Tenzer, S., Wichert, S. P., Patzig, J., & Werner, H. B. (2012). Systematic approaches to central nervous system myelin. *Cellular and Molecular Life Sciences*, *69*(17), 2879–2894. https://doi.org/10.1007/s00018-012-0958-9

de Monasterio-Schrader, P., Patzig, J., Möbius, W., Barrette, B., Wagner, T. L., Kusch, K., Edgar, J. M., Brophy, P. J., & Werner, H. B. (2013). Uncoupling of neuroinflammation from axonal degeneration in mice lacking the myelin protein tetraspanin-2. *GLIA*, *61*, 1832–1847. https://doi.org/10.1002/glia.22561

824 Deerinck, T. J., Bushong, E. A., Thor, A., & Ellisman, M. H. (2010). Ncmir methods for 3D
825 EM: A New protocol for preparation of biological specimens for serial block face
826 scanning electron microscopy. *Microscopy*, 6–8.
827 http://scholar.google.com/scholar?start=320&q=Mark+Ellisman&hl=en&as_sdt=0,5#0

828 di Stefano, M., Nascimento-Ferreira, I., Orsomando, G., Mori, V., Gilley, J., Brown, R.,
829 Janeckova, L., Vargas, M. E., Worrell, L. A., Loreto, A., Tickle, J., Patrick, J., Webster,
830 J. R. M., Marangoni, M., Carpi, F. M., Pucciarelli, S., Rossi, F., Meng, W., Sagasti, A.,
831 … Conforti, L. (2015). A rise in NAD precursor nicotinamide mononucleotide (NMN)
832 after injury promotes axon degeneration. *Cell Death and Differentiation*, *22*(5), 731–742.
833 https://doi.org/10.1038/cdd.2014.164

834 Dieck, S. T., Specht, D., Strenzke, N., Hida, Y., Krishnamoorthy, V., Schmidt, K. F., Inoue,
835 E., Ishizaki, H., Tanaka-Okamoto, M., Miyoshi, J., Hagiwara, A., Brandstatter, J. H.,
836 Löwel, S., Gollisch, T., Ohtsuka, T., & Moser, T. (2012). Deletion of the presynaptic
837 scaffold cast reduces active zone size in rod photoreceptors and impairs visual
838 processing. *Journal of Neuroscience*, *32*(35), 12192–12203.
839 https://doi.org/10.1523/JNEUROSCI.0752-12.2012

840 Distler, U., Kuharev, J., Navarro, P., Levin, Y., Schild, H., & Tenzer, S. (2014). Drift time-
841 specific collision energies enable deep-coverage data-independent acquisition
842 proteomics. *Nature Methods*, *11*(2), 167–170. https://doi.org/10.1038/nmeth.2767

843 Edgar, J. M., McLaughlin, M., Werner, H. B., McCulloch, M. C., Barrie, J. A., Brown, A.,
844 Faichney, A. B., Snaidero, N., Nave, K. A., & Griffiths, I. R. (2009). Early ultrastructural
845 defects of axons and axon-glia junctions in mice lacking expression of Cnp1. *GLIA*,
846 *57*(16), 1815–1824. https://doi.org/10.1002/glia.20893

847 Edgar, J. M., McLaughlin, M., Yool, D., Zhang, S. C., Fowler, J. H., Montague, P., Barrie, J.
848 A., McCulloch, M. C., Duncan, I. D., Garbern, J., Nave, K. A., & Griffiths, I. R. (2004).
849 Oligodendroglial modulation of fast axonal transport in a mouse model of hereditary
850 spastic paraplegia. *Journal of Cell Biology*, *166*(1), 121–131.
851 https://doi.org/10.1083/jcb.200312012

852 Eichel, M. A., Gargareta, V. I., D'Este, E., Fledrich, R., Kungl, T., Buscham, T. J., Lüders, K.
853 A., Miracle, C., Jung, R. B., Distler, U., Kusch, K., Möbius, W., Hülsmann, S., Tenzer,
854 S., Nave, K. A., & Werner, H. B. (2020). CMTM6 expressed on the adaxonal Schwann
855 cell surface restricts axonal diameters in peripheral nerves. *Nature Communications*,
856 *11*(1), 4514. https://doi.org/10.1038/s41467-020-18172-7

857 Erwig, M. S., Hesse, D., Jung, R. B., Uecker, M., Kusch, K., Tenzer, S., Jahn, O., & Werner,
858 H. B. (2019). Myelin: Methods for purification and proteome analysis. *Methods in*
859 *Molecular Biology*, *1936*, 37–63. https://doi.org/10.1007/978-1-4939-9072-6_3

860 Erwig, M. S., Patzig, J., Steyer, A. M., Dibaj, P., Heilmann, M., Heilmann, I., Jung, R. B.,
861 Kusch, K., Möbius, W., Jahn, O., Nave, K.-A., & Werner, H. B. (2019). Anillin facilitates
862 septin assembly to prevent pathological outfoldings of central nervous system myelin.
863 *ELife*, *8*, e43888. https://doi.org/10.7554/eLife.43888.001

864 Fadnavis, S., Batson, J., & Garyfallidis, E. (2020). *Patch2Self: Denoising Diffusion MRI with*
865 *Self-Supervised Learning*. http://arxiv.org/abs/2011.01355

Farley, F. W., Soriano, P., Steffen, L. S., & Dymecki, S. M. (2000). Widespread Recombinase Expression Using FLPeR (Flipper) Mice. *Genesis*, *28*, 106–110.

Franklin, R. J. M., Ffrench-Constant, C., Edgar, J. M., & Smith, K. J. (2012). Neuroprotection and repair in multiple sclerosis. *Nature Reviews Neurology*, *8*(11), 624–634. https://doi.org/10.1038/nrneurol.2012.200

Frühbeis, C., Kuo-Elsner, W. P., Müller, C., Barth, K., Peris, L., Tenzer, S., Möbius, W., Werner, H. B., Nave, K. A., Fröhlich, D., & Krämer-Albers, E. M. (2020). Oligodendrocytes support axonal transport and maintenance via exosome secretion. *PLoS Biology*, *18*, e3000621. https://doi.org/10.1371/journal.pbio.3000621

Fünfschilling, U., Supplie, L. M., Mahad, D., Boretius, S., Saab, A. S., Edgar, J., Brinkmann, B. G., Kassmann, C. M., Tzvetanova, I. D., Möbius, W., Diaz, F., Meijer, D., Suter, U., Hamprecht, B., Sereda, M. W., Moraes, C. T., Frahm, J., Goebbels, S., & Nave, K. A. (2012). Glycolytic oligodendrocytes maintain myelin and long-term axonal integrity. *Nature*, *485*(7399), 517–521. https://doi.org/10.1038/nature11007

Garyfallidis, E., Brett, M., Amirbekian, B., Rokem, A., van der Walt, S., Descoteaux, M., & Nimmo-Smith, I. (2014). Dipy, a library for the analysis of diffusion MRI data. *Frontiers in Neuroinformatics*, *8*(18). https://doi.org/10.3389/fninf.2014.00008

Gerdts, J., Summers, D. W., Sasaki, Y., DiAntonio, A., & Milbrandt, J. (2013). Sarm1-mediated axon degeneration requires both SAM and TIR interactions. *Journal of Neuroscience*, *33*(33), 13569–13580. https://doi.org/10.1523/JNEUROSCI.1197-13.2013

Ghandour, M. S., Vincendon, G., Gombos, A., Limozin, N., Filippi, D., Dalmasso, C., & Laurent, G. (1980). Carbonic Anhydrase and Oligodendroglia in Developing Rat Cerebellum: A Biochemical and Immunohistological Study. *Developmental Biology*, *77*, 73–83.

Gilley, J., & Coleman, M. P. (2010). Endogenous Nmnat2 Is an Essential Survival Factor for Maintenance of Healthy Axons. *PLoS Biology*, *8*(1), e1000300. https://doi.org/10.1371/journal.pbio.1000300

Gong, S., Doughty, M., Harbaugh, C. R., Cummins, A., Hatten, M. E., Heintz, N., & Gerfen, C. R. (2007). Targeting Cre recombinase to specific neuron populations with bacterial artificial chromosome constructs. *Journal of Neuroscience*, *27*(37), 9817–9823. https://doi.org/10.1523/JNEUROSCI.2707-07.2007

Griffiths I, Klugmann M, Anderson T, Thomson C, Vouyiouklis D, & Nave KA. (1998). Axonal swellings and degeneration in mice lacking the major proteolipid of myelin. *Science*, *280*, 1610–1613.

Hagemeyer, N., Goebbels, S., Papiol, S., Kästner, A., Hofer, S., Begemann, M., Gerwig, U. C., Boretius, S., Wieser, G. L., Ronnenberg, A., Gurvich, A., Heckers, S. H., Frahm, J., Nave, K. A., & Ehrenreich, H. (2012). A myelin gene causative of a catatonia-depression syndrome upon aging. *EMBO Molecular Medicine*, *4*(6), 528–539. https://doi.org/10.1002/emmm.201200230

Han, W., Ding, P., Xu, M., Wang, L., Rui, M., Shi, S., Liu, Y., Zheng, Y., Chen, Y., Yang, T., & Ma, D. (2003). Identification of eight genes encoding chemokine-like factor

superfamily members 1-8 (CKLFSF1-8) by in silico cloning and experimental validation. *Genomics*, *81*(6), 609–617. https://doi.org/10.1016/S0888-7543(03)00095-8

Hartline, D. K., & Colman, D. R. (2007). Rapid Conduction and the Evolution of Giant Axons and Myelinated Fibers. *Current Biology*, *17*(1), 29–35. https://doi.org/10.1016/j.cub.2006.11.042

Helms, G., Dathe, H., Kallenberg, K., & Dechent, P. (2008). High-resolution maps of magnetization transfer with inherent correction for RF inhomogeneity and T1 relaxation obtained from 3D FLASH MRI. *Magnetic Resonance in Medicine*, *60*(6), 1396–1407. https://doi.org/10.1002/mrm.21732

Hopkins, E. L., Gu, W., Kobe, B., & Coleman, M. P. (2021). A Novel NAD Signaling Mechanism in Axon Degeneration and its Relationship to Innate Immunity. *Frontiers in Molecular Biosciences*, *8*, 703532. https://doi.org/10.3389/fmolb.2021.703532

Hughes, R. O., Bosanac, T., Mao, X., Engber, T. M., DiAntonio, A., Milbrandt, J., Devraj, R., & Krauss, R. (2021). Small Molecule SARM1 Inhibitors Recapitulate the SARM1−/− Phenotype and Allow Recovery of a Metastable Pool of Axons Fated to Degenerate. *Cell Reports*, *34*(1), 108588. https://doi.org/10.1016/j.celrep.2020.108588

Ishii, A., Dutta, R., Wark, G. M., Hwang, S.-I., Han, D. K., Trapp, B. D., Pfeiffer, S. E., & Bansal, R. (2009). Human myelin proteome and comparative analysis with mouse myelin. *PNAS*, *106*(34), 14605–14610. www.pnas.org/cgi/content/full/

Jahn, O., Siems, S. B., Kusch, K., Hesse, D., Jung, R. B., Liepold, T., Uecker, M., Sun, T., & Werner, H. B. (2020). The CNS Myelin Proteome: Deep Profile and Persistence After Post-mortem Delay. *Frontiers in Cellular Neuroscience*, *14*, 239. https://doi.org/10.3389/fncel.2020.00239

Jäkel, S., Agirre, E., Mendanha Falcão, A., van Bruggen, D., Lee, K. W., Knuesel, I., Malhotra, D., ffrench-Constant, C., Williams, A., & Castelo-Branco, G. (2019). Altered human oligodendrocyte heterogeneity in multiple sclerosis. *Nature*, *566*(7745), 543–547. https://doi.org/10.1038/s41586-019-0903-2

Jumper, J., Evans, R., Pritzel, A., Green, T., Figurnov, M., Ronneberger, O., Tunyasuvunakool, K., Bates, R., Žídek, A., Potapenko, A., Bridgland, A., Meyer, C., Kohl, S. A. A., Ballard, A. J., Cowie, A., Romera-Paredes, B., Nikolov, S., Jain, R., Adler, J., … Hassabis, D. (2021). Highly accurate protein structure prediction with AlphaFold. *Nature*, *596*(7873), 583–589. https://doi.org/10.1038/s41586-021-03819-2

Jung, M., Sommer, I., Schachner, M., & Nave, K.-A. (1996). Monoclonal Antibody O10 Defines a Conformationally Sensitive Cell-Surface Epitope of Proteolipid Protein (PLP): Evidence that PLP Misfolding Underlies Dysmyelination in Mutant Mice. *The Journal of Neuroscience*, *16*(24), 7920–7929.

Kagawa, T., Mekada, E., Shishido, Y., & Ikenaka, K. (1997). Immune System-Related CD9 Is Expressed in Mouse Central Nervous System Myelin at a Very Late Stage of Myelination. *J. Neurosci. Res*, *50*, 312–320.

Kleopa, K. A., Orthmann, J. L., Enriquez, A., Paul, D. L., & Scherer, S. S. (2004). Unique distributions of the gap junction proteins connexin29, connexin32, and connexin47 in oligodendrocytes. *GLIA*, *47*(4), 346–357. https://doi.org/10.1002/glia.20043

950 Klugmann, M., & Schwab, M. H. (1997). Assembly of CNS Myelin in the Absence of
951 Proteolipid Protein. *Neuron*, *18*, 59–70.

952 Kuharev, J., Navarro, P., Distler, U., Jahn, O., & Tenzer, S. (2015). In-depth evaluation of
953 software tools for data-independent acquisition based label-free quantification.
954 *Proteomics*, *15*(18), 3140–3151. https://doi.org/10.1002/pmic.201400396

955 Lappe-Siefke, C., Goebbels, S., Gravel, M., Nicksch, E., Lee, J., Braun, P. E., Griffiths, I. R.,
956 & Navel, K. A. (2003). Disruption of Cnp1 uncouples oligodendroglial functions in axonal
957 support and myelination. *Nature Genetics*, *33*(3), 366–374.
958 https://doi.org/10.1038/ng1095

959 Lee, Y., Morrison, B. M., Li, Y., Lengacher, S., Farah, M. H., Hoffman, P. N., Liu, Y.,
960 Tsingalia, A., Jin, L., Zhang, P. W., Pellerin, L., Magistretti, P. J., & Rothstein, J. D.
961 (2012). Oligodendroglia metabolically support axons and contribute to
962 neurodegeneration. *Nature*, *487*(7408), 443–448. https://doi.org/10.1038/nature11314

963 Leone, D. P., Genoud, S., Atanasoski, S., Grausenburger, R., Berger, P., Metzger, D.,
964 Macklin, W. B., Chambon, P., & Suter, U. (2003). Tamoxifen-inducible glia-specific Cre
965 mice for somatic mutagenesis in oligodendrocytes and Schwann cells. *Molecular and*
966 *Cellular Neuroscience*, *22*(4), 430–440. https://doi.org/10.1016/S1044-7431(03)00029-0

967 Loring, H. S., Parelkar, S. S., Mondal, S., & Thompson, P. R. (2020). Identification of the first
968 noncompetitive SARM1 inhibitors. *Bioorganic and Medicinal Chemistry*, *28*(18), 115644.
969 https://doi.org/10.1016/j.bmc.2020.115644

970 Lüders, K. A., Nessler, S., Kusch, K., Patzig, J., Jung, R. B., Möbius, W., Nave, K. A., &
971 Werner, H. B. (2019). Maintenance of high proteolipid protein level in adult central
972 nervous system myelin is required to preserve the integrity of myelin and axons. *GLIA*,
973 *67*(4), 634–649. https://doi.org/10.1002/glia.23549

974 Lüders, K. A., Patzig, J., Simons, M., Nave, K. A., & Werner, H. B. (2017). Genetic dissection
975 of oligodendroglial and neuronal Plp1 function in a novel mouse model of spastic
976 paraplegia type 2. *GLIA*, *65*(11), 1762–1776. https://doi.org/10.1002/glia.23193

977 Lunn, E. R., Perry, V. H., Brown, M. C., & Gordon', S. (1989). Absence of Wallerian
978 Degeneration does not Hinder Regeneration in Peripheral Nerve. *European Journal of*
979 *Neuroscience*, *I*(1), 27–33.

980 Mack, T. G. A., Reiner, M., Beirowski, B., Mi, W., Emanuelli, M., Wagner, D., Thomson, D.,
981 Gillingwater, T., Court, F., Conforti, L., Fernando, F. S., Tarlton, A., Andressen, C.,
982 Addicks, K., Magni, G., Ribchester, R. R., Perry, V. H., & Coleman, M. P. (2001).
983 Wallerian degeneration of injured axons and synapses is delayed by a Ube4b/Nmnat
984 chimeric gene. *Nature Neuroscience*, *4*(12), 1199–1206. https://doi.org/10.1038/nn770

985 Mezzadra, R., Sun, C., Jae, L. T., Gomez-Eerland, R., de Vries, E., Wu, W., Logtenberg, M.
986 E. W., Slagter, M., Rozeman, E. A., Hofland, I., Broeks, A., Horlings, H. M., Wessels, L.
987 F. A., Blank, C. U., Xiao, Y., Heck, A. J. R., Borst, J., Brummelkamp, T. R., &
988 Schumacher, T. N. M. (2017). Identification of CMTM6 and CMTM4 as PD-L1 protein
989 regulators. *Nature*, *549*(7670), 106–110. https://doi.org/10.1038/nature23669

990 Möbius, W., Cooper, B., Kaufmann, W. A., Imig, C., Ruhwedel, T., Snaidero, N., Saab, A. S.,
991 & Varoqueaux, F. (2010). Electron microscopy of the mouse central nervous system.

Methods in Cell Biology, *96*(C), 475–512. https://doi.org/10.1016/S0091-679X(10)96020-2

Mukherjee, C., Kling, T., Russo, B., Miebach, K., Kess, E., Schifferer, M., Pedro, L. D., Weikert, U., Fard, M. K., Kannaiyan, N., Rossner, M., Aicher, M. L., Goebbels, S., Nave, K. A., Krämer-Albers, E. M., Schneider, A., & Simons, M. (2020). Oligodendrocytes Provide Antioxidant Defense Function for Neurons by Secreting Ferritin Heavy Chain. *Cell Metabolism*, *32*(2), 259-272.e10. https://doi.org/10.1016/j.cmet.2020.05.019

Osterloh, J. M., Yang, J., Rooney, T. M., Fox, A. N., Adalbert, R., Powell, E. H., Sheehan, A. E., Avery, M. A., Hackett, R., Logan, M. A., MacDonald, J. M., Ziegenfuss, J. S., Milde, S., Hou, Y. J., Nathan, C., Ding, A., Brown, R. H., Conforti, L., Coleman, M., … Freeman, M. R. (2012). dSarm/Sarm1 is required for activation of an injury-induced axon death pathway. *Science*, *337*(6093), 481–484. https://doi.org/10.1126/science.1223899

Ou, X., Sun, S. W., Liang, H. F., Song, S. K., & Gochberg, D. F. (2009). Quantitative magnetization transfer measured pool-size ratio reflects optic nerve myelin content in Ex vivo mice. *Magnetic Resonance in Medicine*, *61*(2), 364–371. https://doi.org/10.1002/mrm.21850

Patzig, J., Erwig, M. S., Tenzer, S., Kusch, K., Dibaj, P., Möbius, W., Goebbels, S., Schaeren-Wiemers, N., Nave, K. A., & Werner, H. B. (2016). Septin/anillin filaments scaffold central nervous system myelin to accelerate nerve conduction. *ELife*, *5*, e17119. https://doi.org/10.7554/eLife.17119.001

Pei, M., Nguyen, T. D., Thimmappa, N. D., Salustri, C., Dong, F., Cooper, M. A., Li, J., Prince, M. R., & Wang, Y. (2015). Algorithm for fast monoexponential fitting based on Auto-Regression on Linear Operations (ARLO) of data. *Magnetic Resonance in Medicine*, *73*(2), 843–850. https://doi.org/10.1002/mrm.25137

Perez-Riverol, Y., Csordas, A., Bai, J., Bernal-Llinares, M., Hewapathirana, S., Kundu, D. J., Inuganti, A., Griss, J., Mayer, G., Eisenacher, M., Pérez, E., Uszkoreit, J., Pfeuffer, J., Sachsenberg, T., Yilmaz, Ş., Tiwary, S., Cox, J., Audain, E., Walzer, M., … Vizcaíno, J. A. (2019). The PRIDE database and related tools and resources in 2019: Improving support for quantification data. *Nucleic Acids Research*, *47*(D1), D442–D450. https://doi.org/10.1093/nar/gky1106

Philips, T., Mironova, Y. A., Jouroukhin, Y., Chew, J., Vidensky, S., Farah, M. H., Pletnikov, M. v., Bergles, D. E., Morrison, B. M., & Rothstein, J. D. (2021). MCT1 Deletion in Oligodendrocyte Lineage Cells Causes Late-Onset Hypomyelination and Axonal Degeneration. *Cell Reports*, *34*(2), 108610. https://doi.org/10.1016/j.celrep.2020.108610

Provencher, S. W. (1993). Estimation of Metabolite Concentrations from Localized in Vivo Proton NMR Spectra. In *Magnetic Resonance in Medicine* (Vol. 30, pp. 672–679).

Rasband, M. N., Tayler, J., Kaga, Y., Yang, Y., Lappe-Siefke, C., Nave, K. A., & Bansal, R. (2005). CNP is required for maintenance of axon-glia interactions at nodes of ranvier in the CNS. *GLIA*, *50*(1), 86–90. https://doi.org/10.1002/glia.20165

Ridder, W. H., & Nusinowitz, S. (2006). The visual evoked potential in the mouse - Origins and response characteristics. *Vision Research*, *46*(6–7), 902–913. https://doi.org/10.1016/j.visres.2005.09.006

1035 Roach, A., Takahashi, N., Pravtcheva, D., Ruddle, F., & Hood, L. (1985). Chromosomal
1036 Mapping of Mouse Myelin Basic Protein Gene and Structure and Transcription of the
1037 Partially Deleted Gene in Shiverer Mutant Mice. *Cell*, *42*, 149–155.

1038 Saab, A. S., Tzvetavona, I. D., Trevisiol, A., Baltan, S., Dibaj, P., Kusch, K., Möbius, W.,
1039 Goetze, B., Jahn, H. M., Huang, W., Steffens, H., Schomburg, E. D., Pérez-Samartín,
1040 A., Pérez-Cerdá, F., Bakhtiari, D., Matute, C., Löwel, S., Griesinger, C., Hirrlinger, J., …
1041 Nave, K. A. (2016). Oligodendroglial NMDA Receptors Regulate Glucose Import and
1042 Axonal Energy Metabolism. *Neuron*, *91*(1), 119–132.
1043 https://doi.org/10.1016/j.neuron.2016.05.016

1044 Samsam, M., Mi, W., Wessig, C., Zielasek, J., Toyka, K. v, Coleman, M. P., & Martini, R.
1045 (2003). The Wlds Mutation Delays Robust Loss of Motor and Sensory Axons in a
1046 Genetic Model for Myelin-Related Axonopathy. *The Journal of Neuroscience*, *23*(7),
1047 2833–2839.

1048 Schardt, A., Brinkmann, B. G., Mitkovski, M., Sereda, M. W., Werner, H. B., & Nave, K. A.
1049 (2009). The SNARE protein SNAP-29 interacts with the GTPase Rab3A: Implications for
1050 membrane trafficking in myelinating glia. *Journal of Neuroscience Research*, *87*(15),
1051 3465–3479. https://doi.org/10.1002/jnr.22005

1052 Schindelin, J., Arganda-Carreras, I., Frise, E., Kaynig, V., Longair, M., Pietzsch, T.,
1053 Preibisch, S., Rueden, C., Saalfeld, S., Schmid, B., Tinevez, J. Y., White, D. J.,
1054 Hartenstein, V., Eliceiri, K., Tomancak, P., & Cardona, A. (2012). Fiji: An open-source
1055 platform for biological-image analysis. *Nature Methods*, *9*(7), 676–682.
1056 https://doi.org/10.1038/nmeth.2019

1057 Shao, L., Cui, Y., Li, H., Liu, Y., Zhao, H., Wang, Y., Zhang, Y., Ka, M. N., Han, W., Ma, D., &
1058 Tao, Q. (2007). CMTM5 exhibits tumor suppressor activities and is frequently silenced
1059 by methylation in carcinoma cell lines. *Clinical Cancer Research*, *13*(19), 5756–5762.
1060 https://doi.org/10.1158/1078-0432.CCR-06-3082

1061 Siems, S. B., Jahn, O., Eichel, M. A., Kannaiyan, N., Wu, L. M. N., Sherman, D. L., Kusch,
1062 K., Hesse, D., Jung, R. B., Fledrich, R., Sereda, M. W., Rossner, M. J., Brophy, P. J., &
1063 Werner, H. B. (2020). Proteome profile of peripheral myelin in healthy mice and in a
1064 neuropathy model. *ELife*, *9*, e51406. https://doi.org/10.7554/eLife.51406

1065 Silva, J. C., Gorenstein, M. v., Li, G. Z., Vissers, J. P. C., & Geromanos, S. J. (2006).
1066 Absolute quantification of proteins by LCMSE: A virtue of parallel MS acquisition.
1067 *Molecular and Cellular Proteomics*, *5*(1), 144–156.
1068 https://doi.org/10.1074/mcp.M500230-MCP200

1069 Stadelmann, C., Timmler, S., Barrantes-Freer, A., & Simons, M. (2019). Myelin in the Central
1070 Nervous System: Structure, Function, and Pathology. *Physiol Rev*, *99*, 1381–1431.
1071 https://doi.org/10.1152/physrev.00031.2018.-Oligodendro

1072 Steyer, A. M., Ruhwedel, T., Nardis, C., Werner, H. B., Nave, K. A., & Möbius, W. (2020).
1073 Pathology of myelinated axons in the PLP-deficient mouse model of spastic paraplegia
1074 type 2 revealed by volume imaging using focused ion beam-scanning electron
1075 microscopy. *Journal of Structural Biology*, *210*(2), 107492.
1076 https://doi.org/10.1016/j.jsb.2020.107492

1077 Tasaki, I. (1939). The electro-saltatory transmission of the nerve impulse and the effect of
1078 narcosis upon the nerve fiber. *The American Journal of Physiology*, *127*(2), 211–227.
1079 https://doi.org/10.1152/AJPLEGACY.1939.127.2.211

1080 Trevisiol, A., Kusch, K., Steyer, A. M., Gregor, I., Nardis, C., Winkler, U., Köhler, S.,
1081 Restrepo, A., Möbius, W., Werner, H. B., Nave, K. A., & Hirrlinger, J. (2020). Structural
1082 myelin defects are associated with low axonal ATP levels but rapid recovery from
1083 energy deprivation in a mouse model of spastic paraplegia. *PLoS Biology*, *18*(11),
1084 e3000943. https://doi.org/10.1371/journal.pbio.3000943

1085 Uschkureit, T., Spörkel, O., Stracke, J., Bü, H., & Stoffel, W. (2000). Early Onset of Axonal
1086 Degeneration in Double (plp/mag/) and Hypomyelinosis in Triple (plp/mbp/mag/) Mutant
1087 Mice. *The Journal of Neuroscience*, *20*(14), 5225–5233.

1088 Wang, J., Zhai, Q., Chen, Y., Lin, E., Gu, W., McBurney, M. W., & He, Z. (2005). A local
1089 mechanism mediates NAD-dependent protection of axon degeneration. *Journal of Cell*
1090 *Biology*, *170*(3), 349–355. https://doi.org/10.1083/jcb.200504028

1091 Weil, M. T., Heibeck, S., Töpperwien, M., Tom Dieck, S., Ruhwedel, T., Salditt, T., Rodicio,
1092 M. C., Morgan, J. R., Nave, K. A., Möbius, W., & Werner, H. B. (2018). Axonal
1093 ensheathment in the nervous system of lamprey: Implications for the evolution of
1094 myelinating glia. *Journal of Neuroscience*, *38*(29), 6586–6596.
1095 https://doi.org/10.1523/JNEUROSCI.1034-18.2018

1096 Werner, H. B., Krämer-Albers, E. M., Strenzke, N., Saher, G., Tenzer, S., Ohno-Iwashita, Y.,
1097 de Monasterio-Schrader, P., Möbius, W., Moser, T., Griffiths, I. R., & Nave, K. A. (2013).
1098 A critical role for the cholesterol-associated proteolipids PLP and M6B in myelination of
1099 the central nervous system. *GLIA*, *61*(4), 567–586. https://doi.org/10.1002/glia.22456

1100 Wieser, G. L., Gerwig, U. C., Adamcio, B., Barrette, B., Nave, K. A., Ehrenreich, H., &
1101 Goebbels, S. (2013). Neuroinflammation in white matter tracts of Cnp1 mutant mice
1102 amplified by a minor brain injury. *GLIA*, *61*(6), 869–880.
1103 https://doi.org/10.1002/glia.22480

1104 Wolf, N. I., ffrench-Constant, C., & van der Knaap, M. S. (2021). Hypomyelinating
1105 leukodystrophies — unravelling myelin biology. *Nature Reviews Neurology*, *17*(2), 88–
1106 103. https://doi.org/10.1038/s41582-020-00432-1

1107 Xiao, Y., Yuan, Y., Zhang, Y., Li, J., Liu, Z., Zhang, X., Sheng, Z., Xu, T., & Wang, X. (2015).
1108 CMTM5 is reduced in prostate cancer and inhibits cancer cell growth in vitro and in vivo.
1109 *Clinical and Translational Oncology*, *17*(6), 431–437. https://doi.org/10.1007/s12094-
1110 014-1253-z

1111 Yuan, Y., Sheng, Z., Liu, Z., Zhang, X., Xiao, Y., Xie, J., Zhang, Y., & Xu, T. (2020). CMTM5-
1112 v1 inhibits cell proliferation and migration by downregulating oncogenic EGFR signaling
1113 in prostate cancer cells. *Journal of Cancer*, *11*(13), 3762–3770.
1114 https://doi.org/10.7150/jca.42314

1115 Zhang, Y., Chen, K., Sloan, S. A., Bennett, M. L., Scholze, A. R., O'Keeffe, S., Phatnani, H.
1116 P., Guarnieri, P., Caneda, C., Ruderisch, N., Deng, S., Liddelow, S. A., Zhang, C.,
1117 Daneman, R., Maniatis, T., Barres, B. A., & Wu, J. Q. (2014). An RNA-sequencing
1118 transcriptome and splicing database of glia, neurons, and vascular cells of the cerebral

cortex. *Journal of Neuroscience*, *34*(36), 11929–11947. https://doi.org/10.1523/JNEUROSCI.1860-14.2014

Zhou, Y., Song, W. M., Andhey, P. S., Swain, A., Levy, T., Miller, K. R., Poliani, P. L., Cominelli, M., Grover, S., Gilfillan, S., Cella, M., Ulland, T. K., Zaitsev, K., Miyashita, A., Ikeuchi, T., Sainouchi, M., Kakita, A., Bennett, D. A., Schneider, J. A., … Colonna, M. (2020). Human and mouse single-nucleus transcriptomics reveal TREM2-dependent and TREM2-independent cellular responses in Alzheimer's disease. *Nature Medicine*, *26*(1), 131–142. https://doi.org/10.1038/s41591-019-0695-9

Figure legends

Figure 1: Identification of CMTM5 as a CNS myelin protein.

(A) Immunoblot analysis of CMTM5 in myelin biochemically purified from the brains C57/Bl6 mice at the age of 75 days compared to brain lysate with the same amount of protein loaded onto the gel. Note that CMTM5 is enriched in myelin. Known myelin proteins PLP, CNP and SIRT2 are detected as markers. Shown are three biological replicates.

(B) Immunohistochemistry and confocal microscopy of spinal cord sections of mice at the age of 75 days. Note that CMTM5 (magenta) labelling was consistent with localization in myelin surrounding beta-III tubulin (TUJ1)-immunopositive axons (yellow) in CTRL (*Cmtm5*$^{fl/fl}$) mice. CMTM5 labelling was not detected in myelin of mice lacking *Cmtm5* expression in mature oligodendrocytes (*Cmtm5*$^{fl/fl}$**Cnp*$^{Cre/Wt}$, cKO). Scale bar, 2 µm.

(C, D) Immunoblot analysis of CMTM5 in brain lysate **(C)** and biochemically purified myelin **(D)** of young and aged mice. Note that CMTM5 abundance in brain lysate increases coinciding with developmental myelination **(D)**. Shown is one biological replicate per age. PLP, CNP, SIRT2 were detected as markers. P= postnatal day, m=months.

Figure 1-Supplement 1: *Cmtm5* mRNA is expressed in mature oligodendrocytes of mice and humans.

(A, B) Abundance of *Cmtm5* mRNA according to bulk RNAseq data of cells immunopanned from mouse cortices (Zhang et al., 2014). Note that among all members of the CMTM family, only *Cmtm5* mRNA is considerably expressed in MOL **(A)**. Increasing *Cmtm5* mRNA expression coincides with maturation of cells of the oligodendrocyte lineage **(B)**. OPC, oligodendrocyte precursor cells; NFO, newly formed oligodendrocyte; MOL, Mature oligodendrocytes; FPKM, fragments per kilobase per million mapped fragments. Data represented as mean ± SEM.

(C, D) Uniform manifold approximation and projection (UMAP) feature plots of scRNAseq data derived from a previously published dataset (Zhou et al., 2020) shows enriched expression of *Cmtm5* mRNA in mature oligodendrocytes (MOL) of mice **(C)**. *Mbp* serves as a marker gene for MOL in mice **(D)**.

(E, F) UMAP feature plots of scRNAseq data derived from a previously published dataset (Jäkel et al., 2019) shows enriched expression of *CMTM5* mRNA in mature oligodendrocytes (MOL) of the white matter in disease-unaffected human control samples **(E)**. *MBP* serves a marker gene for human MOL **(F)**.

Figure 2: CMTM5 is not essential for myelin biogenesis and composition.

(A) Immunoblot analysis shows that CMTM5 is undetectable in myelin purified from the brains of *Cmtm5*$^{fl/fl}$**Cnp*$^{Cre/Wt}$ (cKO) mice. PLP, CNP, SIRT2 were detected as markers. Shown are three biological replicates per genotype.

(B,B') Quantitative proteome analysis of brain myelin reveals largely similar myelin composition in *Cmtm5* cKO and CTRL mice. Analyzed were n=3 mice per genotype and 2 technical replicates per mouse (see **Figure 2B source data 1**). **(B)** Volcano plot with data points representing log2-fold change and -log10-transformed q-values of 428 identified proteins in cKO compared to CTRL myelin. Red dots highlight known myelin proteins. Stippled lines indicate thresholds. CMTM5 is not displayed because it was not identified in *Cmtm5* cKO myelin. **(B')** Heatmap showing the relative abundance of selected known myelin proteins in *Cmtm5* cKO compared to control myelin. Data represents n=3 mice per genotype analyzed as 2 technical replicates per mouse (T1-T6). Note that the relative abundance of most myelin proteins was essentially similar in cKO and CTRL myelin. In agreement with the immunoblot analysis in **(A)** the abundance of CNP was about halved in *Cmtm5* cKO myelin reflecting that the Cre driver line (*Cnp*$^{Cre/Wt}$) possesses only one *Cnp* allele. CMTM5 was not detected (n.d.) in cKO myelin.

(C-L) Electron micrographs and quantitative assessment of myelin in CTRL and cKO optic nerves at postnatal day 30 (P30) **(C-G)** and P75 **(H-L)**. Scale bar, 1µm. Percentage of unmyelinated axons **(D, I)** and pathological myelin profiles is similar between the groups **(E, J)**. Data correspond to all axons (on average more than 1500 axons) from 18-20 non-overlapping random EM images from 4-5 animals per group. Two-tailed Student´s t-test, **D**: p= 0.1003; **E**: p= 0.0598; **I**: p= 0.3937; **J**: p= 0.7269. Mean g-ratio **(F, K)** is similar between the experimental groups at P30 and P75. Data corresponds to 180-200 axons randomly selected from 18-20 EM images for each mouse. n= 4-5 mice per group. Two-tailed Student´s t-test **F**: p= 0.5839; **K**: p= 0.8821. **(G, L)** Scatter plot showing g-ratios in relation to respective axonal diameters. No apparent shift between the experimental groups is detectable.

(M, N) Immunohistochemistry and genotype-dependent quantification of CAII immune-positive oligodendrocytes in a representative white matter tract (hippocampal fimbria) at P75. **(M)** Representative fluorescence micrograph, stippled lines encircle CAII positive cells. Scale bar, 20 µm. **(N)** Number of CAII immunopositive cells number is similar in the fimbria of CTRL and *Cmtm5* cKO mice. n= 5-6 mice per group, unpaired Student´s t-test p= 0.5971. Bar graphs give mean ± SEM; Data points in bar graphs represent induvial mice.

Figure 2-Supplement 1: MRI of the brains of *Cmtm5* cKO mice.

(A) Magnetic resonance imaging (MRI)-based morphometry of brains from CTRL and *Cmtm5* cKO mice at 8 months of age. Shown are representative genotype averaged (4 mice per genotype) effective transverse relaxation rate (R_2^*) MRI images.
(B-E) Diffusion tensor imaging (DTI) indicates unchanged fractional anisotropy (FA), mean diffusivity (MD), axial diffusivity (AD) and radial diffusivity (RD) in white and grey matter in brains of *Cmtm5* cKO and CTRL mice. CC, Corpus callosum; Fim, Fimbria; Thal, Thalamus; Cort, Cortex; AC, Anterior commissure. n=4 per genotype. Precise p-values are given in the statistics section.
(F) Magnetization transfer saturation index (MTsaT) is unaltered in *Cmtm5* cKO compared to CTRL mice. Exact p-values are listed in the statistics section. All graphs give mean ± SEM; all data points represent individual mice.

Figure 2B source data 1. Label-free quantification of proteins in CNS myelin fractions from Cmtm5 cKO and control mice

Identification and quantification data of proteins detected in myelin by DRE-UDMSe. For each of the two conditions, tryptic peptides derived from two technical replicates (replicate digestion) per each of three biological replicates were analyzed by LC-MS (12 runs in total). Proteins (FDR < 1%; 2 peptides/protein) and peptides (FDR < 1%; ≥6 amino acids) were identified by database search against the UniprotKB/SwissProt mouse database using PLGS. Data were post-processed with the software package ISOQuant to calculate absolute in-sample amounts for each detected protein based on the TOP3 approach. Reported abundance values are defined as the relative amount of each protein in respect to the sum over all detected proteins (ppm: parts per million (w/w) of total protein). Typical contaminant proteins like albumin, hemoglobins, and keratins were filtered. The -log10-transformed q-value (column minuslog10q.mod) was plotted against the log2-transformed fold change (column logFC Cmtm5 cKO/CTRL) to obtain the volcano plot shown in Figure 2B. As no imputation of missing values was performed, proteins exclusive for only one of the conditions do not appear in the volcano plot, but are appended at the end of the list. Criteria for statistically significant regulation were as follows: fold change of at least 2.0 (logFC cKO/CTRL > 1) and q-value below 0.01 (minuslog10q.mod > 2.0). Proteins are sorted in descending order for zdist (see column descriptions below).

Figure 3: *Cmtm5* deletion in oligodendrocytes causes axonopathy.

(A-B) Electron micrographs and genotype-dependent quantitative assessment of CTRL and *Cmtm5* cKO optic nerves at P75. Scale bar, 1µm. **(A)** Arrowheads point at pathological axons.

(B) Quantification of pathological profiles reveals progressive axonopathy in optic nerves of *Cmtm5* cKO mice. n=4-5 mice per group, 18-20 random non-overlapping EM images analyzed, Two-tailed Student´s t-test P30 p= 0.0011; P75 p= 0.0191 with Welch´s correction; P365 p<0.0001.

(C) Quantitative assessment of axonal numbers on semithin optic nerve sections. n=4-5 mice per group, data represents mean axon number in five 55 μm^2 rectangles per mouse randomly distributed over the entire optic nerve. Axon numbers are significantly reduced at one year of age according to Two-tailed Student´s t-test P30 p= 0.1288; P75 p= 0.5993; P365 p=0.0499.

(D-E) Electron micrographs and genotype-dependent quantitative assessment of spinal cord white matter in 1 year old CTRL and *Cmtm5* cKO mice. Scale bar= 1µm. **(F)** Number of pathological profiles is increased in spinal cord white matter of *Cmtm5* cKO mice. n=3-7 mice per group, 20 non-overlapping random EM images per mouse, Two-tailed Student´s t-test p=0.0007. All bars show mean ± SEM; all data points represent individual mice.

Figure 3-Supplement 1: *Cmtm5* deletion in oligodendrocytes does not affect the calibers of healthy-appearing axons

(A-C) Quantitative assessment of mean axonal diameters in the optic nerves of *Cmtm5* cKO mice, *Cmtm5*$^{-/-}$ mice and respective controls. Mean axonal diameters are similar between CTRL and cKO mice at ages P75 **(A)** and P365 **(B)** as well as between *Cmtm5*$^{-/-}$ and control mice at age P75 **(C)**. Two-sided Student´s t-test. **A**; p=0.7514, **B**; p= 0.5315, **C**; p= 0.8496. 700-800 optic nerve axons on 18-20 electron micrographs were analyzed per mouse in 4-5 mice per genotype and age. All bars show mean ± SEM; all data points represent individual mice. **(A´-C´)** Frequency distributions of pooled axonal diameters in optic nerves of *Cmtm5* cKO mice, *Cmtm5*$^{-/-}$ mice and respective controls. No apparent shift in axonal diameters was detected between CTRL and cKO mice at ages P75 **(A´)** and P365 **(B´)** as well as between *Cmtm5*$^{-/-}$ and control mice at age P75 **(C´)**. Axonal diameters are the same as used for analysis of mean axonal diameters in **A-C** but represent pools per genotype and timepoint.

Figure 3-Supplement 2: MRS of the corpus callosum of *Cmtm5* cKO mice

(A, B) Spectroscopy of key metabolic markers myo-inositol (for microglia and astrocytes, in **A**) and N-acetyl-aspartate (NAA, for axon/neurons, in **B**). **(A)** The concentration of inositol is significantly increased in the corpus callosum of *Cmtm5* cKO mice compared to controls. Two-tailed Student´s t-test of the mean p= 0.0004. **(B)** NAA levels are unchanged in the corpus callosum of *Cmtm5* cKO mice compared to controls. Two-tailed Student´s t-test of the mean p= 0.057. All bar graphs give mean ± SEM; all data points represent individual mice.

Figure 3-Supplement 3: Secondary neuropathology following *Cmtm5* deletion.
Quantitative assessment of immunohistochemistry detecting neuropathological markers in a representative white matter tract (hippocampal fimbria) using markers for axonal swellings (APP), microglia (MAC3, IBA1) and astroglia (GFAP) at ages P30 **(A-D)**, P75 **(E-H)** and 1 year **(I-L)**. Given is the number of APP-immunopositive axonal swellings **(A, E, I)** the relative area of immunopositivity for MAC3 **(B, F, J)**, IBA1 **(C, G, K)** and GFAP **(D, H, L)**. Note that *Cmtm5* cKO fimbriae display a significant increase of all assessed neuropathological markers at one year of age. n=3-6 mice per group, Two-tailed Student´s t-test **A**: p= 0.3225; **B**: p= 0.7901; **C**: p= 0.9480; **D**; p=0.9152; **E**: p=0.4413; **F**: With Welch´s correction p= 0.0525; **G**: With Welch´s correction p= 0.9049; **H**: p=0.6270; **I**: p= 0.0055; **J**: With Welch´s correction p=0.0251; **K**: With Welch´s correction p<0.0001; **L**: p<0.0001. Bar graphs give mean ± SEM.

Figure 4: FIB-SEM analysis specifies pathological profiles in *Cmtm5* cKO mice.
Focused ion beam-scanning electron microscopy (FIB-SEM) micrographs **(A-D)** and 3-dimensional (3D) reconstruction **(A'-D')** of pathological profiles in *Cmtm5* cKO optic nerve at 1 year of age. **A-C** Scale bar = 1µm. **D** Scale bar = 500 nm. Myelin (cyan), axons (gold), inclusion (purple) and myelin whorls (blue) are highlighted. Pathological profiles include myelin outfoldings, inclusions in the inner tongue, inclusions completely engulfed by axoplasm, and myelin whorls. Analysis of the entire 3D volumes reveals that the relative number of myelin whorls is significantly increased in cKO mice. FIB-SEM stacks of optic nerves of three mice per genotype were analyzed. Normalized volume = 10000µm^3. Two-tailed Student´s t-test **A´´**: p= 0.1882; **B´´**: p= 0.2190; **C´´**: p= 0.2111; **D´´**: p=0.0017. Scale bars 1 µm in **A-C**, 500nm in **D**. Bar graphs give mean ± SEM.

Figure 5: Electroretinography and visual evoked potentials of *Cmtm5* cKO mice
(A-D) Electroretinograms (ERG). **(A)** ERG waveforms in response to light flashes at 0.25 cd-s/m^2 from 11 *Cmtm5* cKO (grand average turquoise, SEM shaded) and 10 CTRL mice (grand average grey, SEM shaded). **(B)** ERG thresholds are similar between CTRL and *Cmtm5* cKO. Unpaired Student´s t-test of the mean ±SEM p= 0.13 **(C,D)** Amplitudes of the ERG A and B waves in response to light flashes of varying intensities in *Cmtm5* cKO (n=11, turquoise) and CTRL mice (n=11, grey; mean ± SEM) are similar between genotypes. 2-way ANOVA **(C)** p= 0.42, **(D)** p= 0.79.

(E-H) Visual evoked potentials (VEP). **(E)** VEP in response to light flashes at 0.01 cd-s/m^2 from 10 *Cmtm5* cKO (grand average turquoise, SEM shaded) and 9 CTRL mice (grand average grey, SEM shaded) display comparable waveforms dominated by a broad negative wave in both genotypes. **(F)** VEP thresholds are not significantly different between CTRL and *Cmtm5* cKO. Unpaired Student´s t-test of the mean ±SEM with Welch´s correction p= 0.33 **(G-H)** VEP latencies and amplitudes in response to light flashes of varying intensities in *Cmtm5* cKO (n=10, turquoise) and CTRL mice (n=8, grey; means ± SEM). Note that *Cmtm5* cKO and CTRL mice show similar VEP latencies but *Cmtm5* cKO mice display reduced VEP amplitudes compared to CTRL mice. 2-way ANOVA **(G)** p= 0.61 **(H)** p= 0.005.

Figure 6: Axonopathy in constitutive and tamoxifen-induced *Cmtm5* mutants.

(A-C) Analysis of mice lacking *Cmtm5* expression from all cells (*Cmtm5*$^{-/-}$ mice) and respective controls. **(A)** Immunoblot confirms absence of CMTM5 in myelin purified from the brains of *Cmtm5*$^{-/-}$ mice. CNP and SIRT2 were detected as controls. **(B)** Representative electron micrographs of *Cmtm5*$^{-/-}$ and respective control optic nerves. Arrowhead points at pathological profile. Scale bar, 1µm. **(C)** Quantitative assessment of 18-20 random non-overlapping EM micrographs from 4-6 mice per group. Note the progressive increase in pathological appearing axons in optic nerves of *Cmtm5*$^{-/-}$ mice. P75: p= 0.0406 by Two-sided Student´s t-test with Welch´s Correction; P365: p< 0.0001 two-sided Student´s t-test.

(D-F) Analysis of mice lacking *Cmtm5* expression in mature oligodendrocytes upon induction by tamoxifen (*Cmtm5*$^{fl/fl}$**Plp*^{CreERT2}, iKO) and respective tamoxifen-injected *Cre*^{ERT2}-negative controls (*Cmtm5*$^{fl/fl}$, CTRL). **(D)** Immunoblot of myelin purified from the brains of mice 4 months post Tamoxifen injection (PTI). Note that the abundance of CMTM5 is strongly reduced in *Cmtm5* iKO myelin. PLP and SIRT2 were detected as controls. **(E)** Representative electron micrographs of *Cmtm5* iKO and CTRL optic nerves. Arrowhead points at pathological profile. Scale bar, 1µm. **(F)** Quantification of pathological profiles (20 non-overlapping random images per mouse, n=5 mice per genotype). Number of pathological profiles is significantly increased 4 months PTI (p=0.0282 by Two-sided Student´s t-test with Welch´s correction). Bar graphs give mean ± SEM; data points represent individual mice.

Figure 6-Supplement 1: Absence of evidence that the abundance of CMTM5 is altered in CNS myelin of *Plp* or *Cnp* deficient mice.

(A, B) Immunoblot analysis of myelin purified from the brains of *Cnp*$^{-/-}$ **(A)** and *Plp*$^{-/Y}$ **(B)** mice and respective controls at P75. Note that the relative abundance of CMTM5 in myelin appears similar. Blots show n=2 mice per genotype. Carbonic anhydrase 2 (CAII) served as control.

Figure 7: Axonopathy upon *Cmtm5* deletion counteracted by the *Wld*^{s} mutation.
(A) Retinae dissected from *Cmtm5* cKO and CTRL mice were immunolabelled with antibodies detecting RBPMS as a marker for Retinal ganglion cells (RGC). Image representative of n=3 retinae. Scale bar= 500 µm. **(B)** Magnification of the inner, middle and outer part of the retina. **(C)** Quantitative assessment indicates that the number of RGCs is similar between *Cmtm5* cKO and CTRL mice. Retinae of 1 year old mice were analyzed. Data represent the mean of 3 non-overlapping areas assessed for each zone (inner, middle outer retina), as indicated by the white boxes in **(A)**. Unpaired Two-sided Student´s t-test inner part: p= 0.8484; middle part: p= 0.5211; outer part: p= 0.2912.
(D-E) Electron micrographs and genotype-dependent quantification of pathological profiles in the optic nerves of *Cmtm5*$^{-/-}$ and control mice in dependence of the *Wld*^{s} mutation at 6 months. Representative electron micrographs; arrowheads point at pathological profiles. Scale bar, 1µm. **(E)** Quantification of pathological profiles in the optic nerves of 6 months old mice. Note that *Cmtm5* deletion causes an increased number of pathological profiles, which is reduced by the presence of the *Wld*^{s} mutation. Data correspond to optic nerves from 4-5 mice per group and 20 random non-overlapping EM images analyzed. Unpaired Two-sided Student´s t-test *Cmtm5*$^{wt/wt}$: p= 0.5107; *Cmtm5*$^{-/-}$: p= 0.0014. Bar graphs give mean ± SEM; data points represent individual mice.

Immunoblot Source data files

Figure 1A source data 1. Immunoblot of CMTM5 in Figure 1A
Figure 1A source data 2. Immunoblot of PLP in Figure 1A
Figure 1A source data 3. Immunoblot of CNP in Figure 1A
Figure 1A source data 4. Immunoblot of SIRT2 in Figure 1A

Figure 1C source data 1. Immunoblot of CMTM5 in Figure 1C at P15-P24 and 6m-24m
Figure 1C source data 2. Immunoblot of PLP in Figure 1C at P15-P24
Figure 1C source data 3. Immunoblot of PLP in Figure 1C at 6m-24m
Figure 1C source data 4. Immunoblot of CNP in Figure 1C at P15-P24
Figure 1C source data 5. Immunoblot of CNP in Figure 1C at 6m-24m
Figure 1C source data 6. Immunoblot of SIRT2 in Figure 1C at P15-P24
Figure 1C source data 7. Immunoblot of SIRT2 in Figure 1C at 6m-24m

Figure 1D source data 1. Immunoblot of CMTM5 in Figure 1D at P15-P24

Figure 1D source data 2. Immunoblot of CMTM5 in Figure 1D at 6m-24m

Figure 1D source data 3. Immunoblot of PLP in Figure 1D at P15-P24

Figure 1D source data 4. Immunoblot of PLP in Figure 1D at 6m-24m

Figure 1D source data 5. Immunoblot of CNP in Figure 1D at P15-P24

Figure 1D source data 6. Immunoblot of CNP in Figure 1D at 6m-24m

Figure 1D source data 7. Immunoblot of SIRT2 in Figure 1D at P15-P24

Figure 1D source data 8. Immunoblot of SIRT2 in Figure 1D at 6m-24m

Figure 2A source data 1. Immunoblot of CMTM5 and SIRT2 in Figure 2A

Figure 2A source data 2. Immunoblot of CNP in Figure 2A

Figure 2A source data 3. Immunoblot of PLP in Figure 2A

Figure 6A source data 1. Immunoblot of CMTM5 in Figure 6A

Figure 6A source data 2. Immunoblot of CNP in Figure 6A

Figure 6A source data 3. Immunoblot of SIRT2 in Figure 6A

Figure 6D source data 1. Immunoblot of CMTM5 in Figure 6D

Figure 6D source data 2. Immunoblot of PLP in Figure 6D

Figure 6D source data 3. Immunoblot of SIRT2 in Figure 6D

Figure 6 Supplement 1A source data 1. Immunoblot of CMTM5 in Figure 6 Supplement 1A

Figure 6 Supplement 1A source data 2. Immunoblot of CAII in Figure 6 Supplement 1A

Figure 6 Supplement 1A source data 3. Immunoblot of CNP in Figure 6 Supplement 1A

Figure 6 Supplement 1B source data 1. Immunoblot of CMTM5 in Figure 6 Supplement 1B

Figure 6 Supplement 1B source data 2. Immunoblot of CAII in Figure 6 Supplement 1B

Figure 6 Supplement 1B source data 3. Immunoblot of PLP in Figure 6 Supplement 1B

Source Data blots labelled. Immunoblots with the relevant bands labelled.

Feature	*Cmtm5* mutants	*Cnp* mutants	*Plp* mutants
Myelinated axons [%]	Normal	Reduced	Reduced
Myelin thickness	Normal	Trend to thinner myelin	Normal-appearing
Myelin structure	Normal	Inner tongue swellings, myelin outfoldings	Lamella splittings, myelin outfoldings
Axonopathy	Early onset, progressive	Early onset, progressive	Early onset, progressive
Modified by Wld^S	Reduction of pathology	No effect	No effect
APP^+ axonal swellings	Late onset	Early onset	Early onset
Microgliosis	Late onset	Early onset	Early onset
Astrogliosis	Late onset	Early onset	Early onset
References	This study	Edgar et al., 2009; Lappe-Siefke et al., 2003; Patzig et al., 2016; Rasband et al., 2005	(Edgar et al., 2004; Griffiths I et al., 1998; Klugmann & Schwab, 1997; Patzig et al., 2016)

Table 1. Comparison of neuropathological features in *Cmtm5*, *Cnp* and *Plp* mutant mice.

Neuropathological features in *Cmtm5* cKO, $Cnp^{-/-}$ and $Plp^{-/Y}$ mutant mice and key references are given. APP, amyloid precursor protein.

Antigen	Host species	Method, dilution	Source and Catalog #
α-APP	Mouse	IHC 1:1000	Chemicon (#MAB348)
α-CAII	Rabbit	IB 1:500, IHC 1:300	(Ghandour et al., 1980)
α-CMTM5	Rabbit	IB 1:1000	Proteintech, Pineda (Custom made) Sequence: YRTELMPSTTEGD
α-CMTM5	Rabbit	IHC 1:200	Pineda (Custom made) Sequence: CAFKIYRTELMPSTTEGDQQ
α-CNP	Mouse	IB 1:1000	Sigma Aldrich (#SAB1405637)
α-GFAP	Mouse	IHC 1:200	Novo Castra (#NCL-L-GFAP-GA5)
α-IBA1	Goat	IHC 1:1000	abcam (#ab5076)
α-MAC3	Rat	IHC 1:400	Pharmingen (#553322)
α-PLP	Rabbit	IB 1:2000	A431, (Jung et al., 1996)
α-RBPMS	Guinea Pig	IHC 1:300	Sigma Aldrich (#ABN1376)
α-SIRT2	Rabbit	IB 1:500	abcam (#ab67299)
α-TUJ1	Mouse	IHC 1:1000	Covance (#MMS-435P)
α-mouse HRP	Goat	IB 1:10000	Dianova (# 115-03-003)
α-rabbit HRP	Goat	IB 1:10000	Dianova (# 111-035-003)
α-rabbit Alexa555	Donkey	IHC 1:1000	Dianova (#SBA-3030-32)
α-guinea pig Alexa555	Donkey	IHC 1:1000	Dianova
α-mouse STAR RED	Goat	IHC 1:200	abberior (# STRED- 1001-500UG)
α-rabbit STAR ORANGE	Goat	IHC 1:200	abberior (# STORANGE-1002-500UG)

Table 2: Antibody information

IHC, immunohistochemistry; IB, immunoblot

Buscham et al., Figure 1

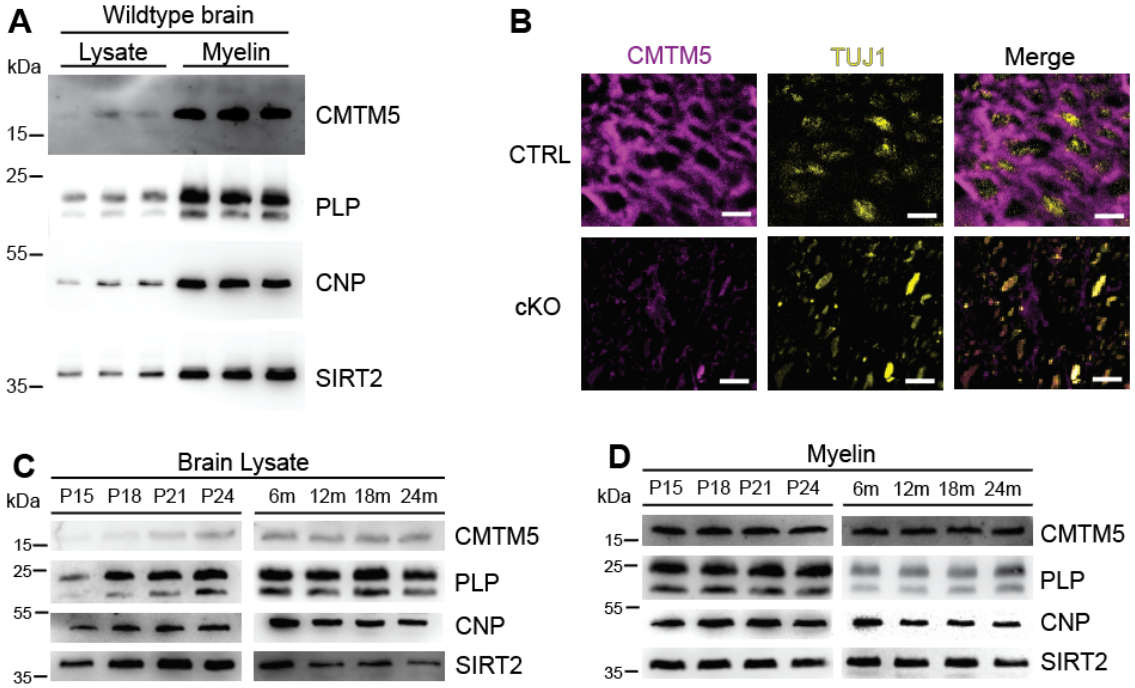

Buscham et al., Figure 1 Supplement 1

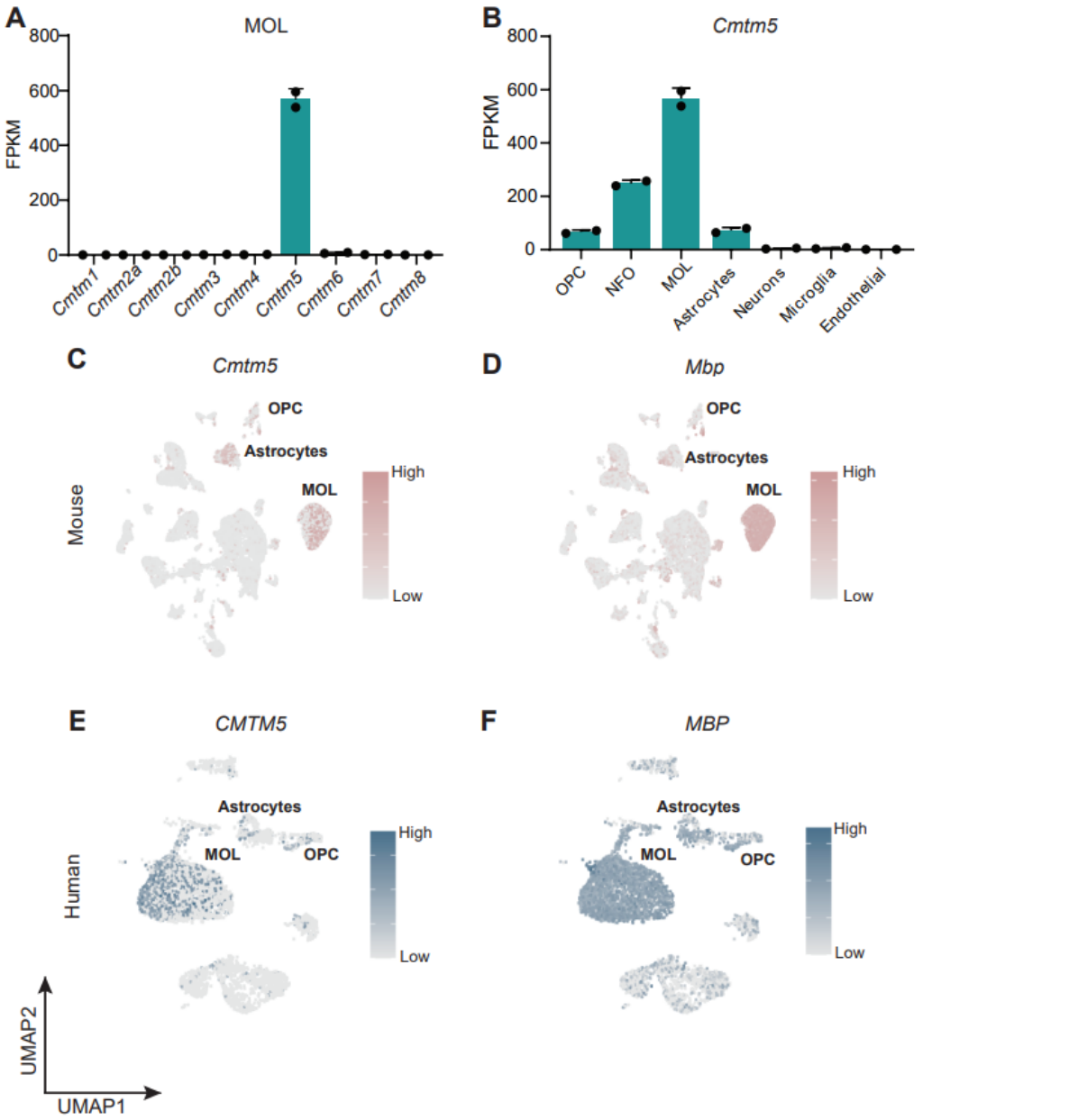

1429

1430

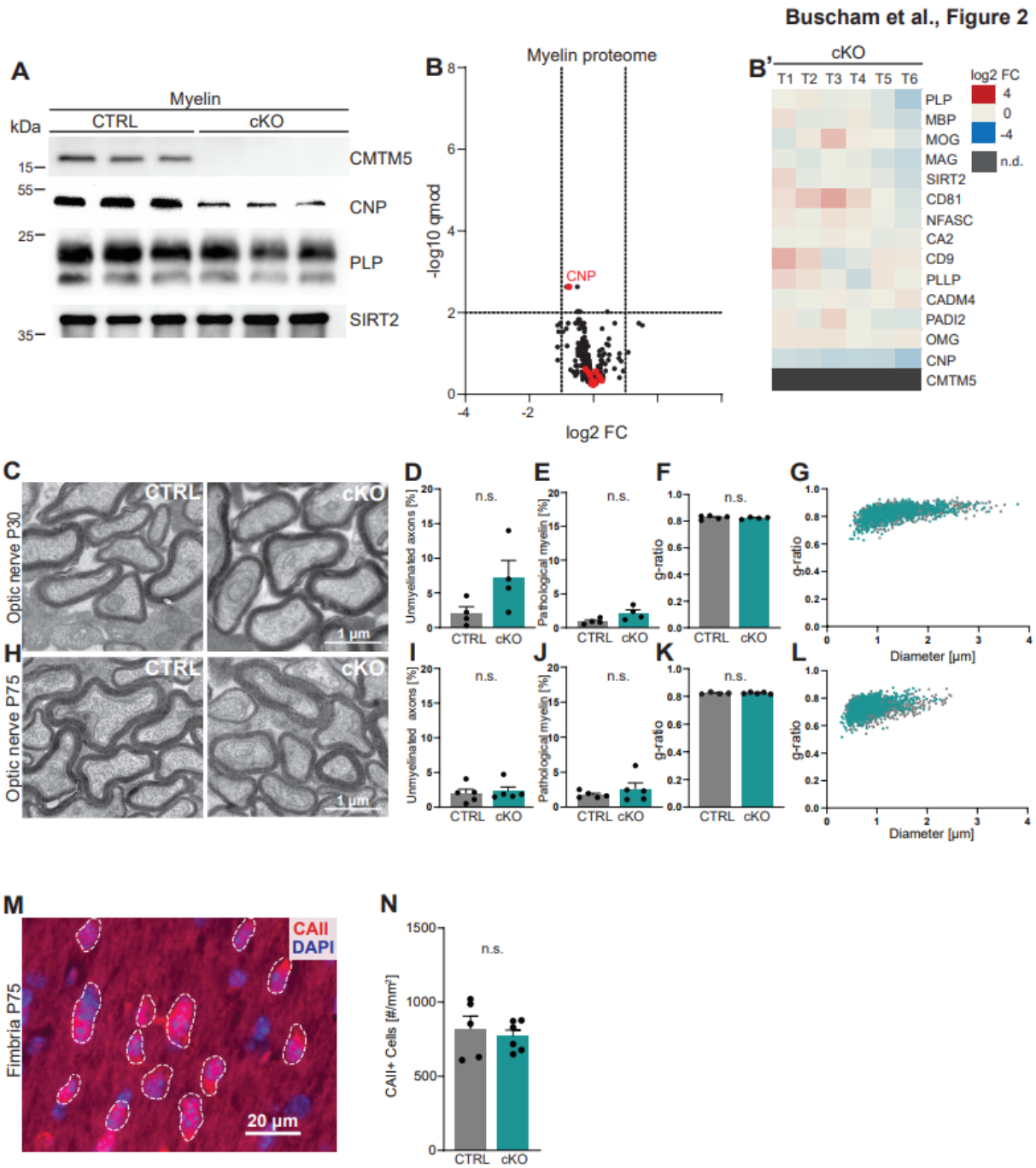

1431

1432

Buscham et al., Figure 2 Supplement 1

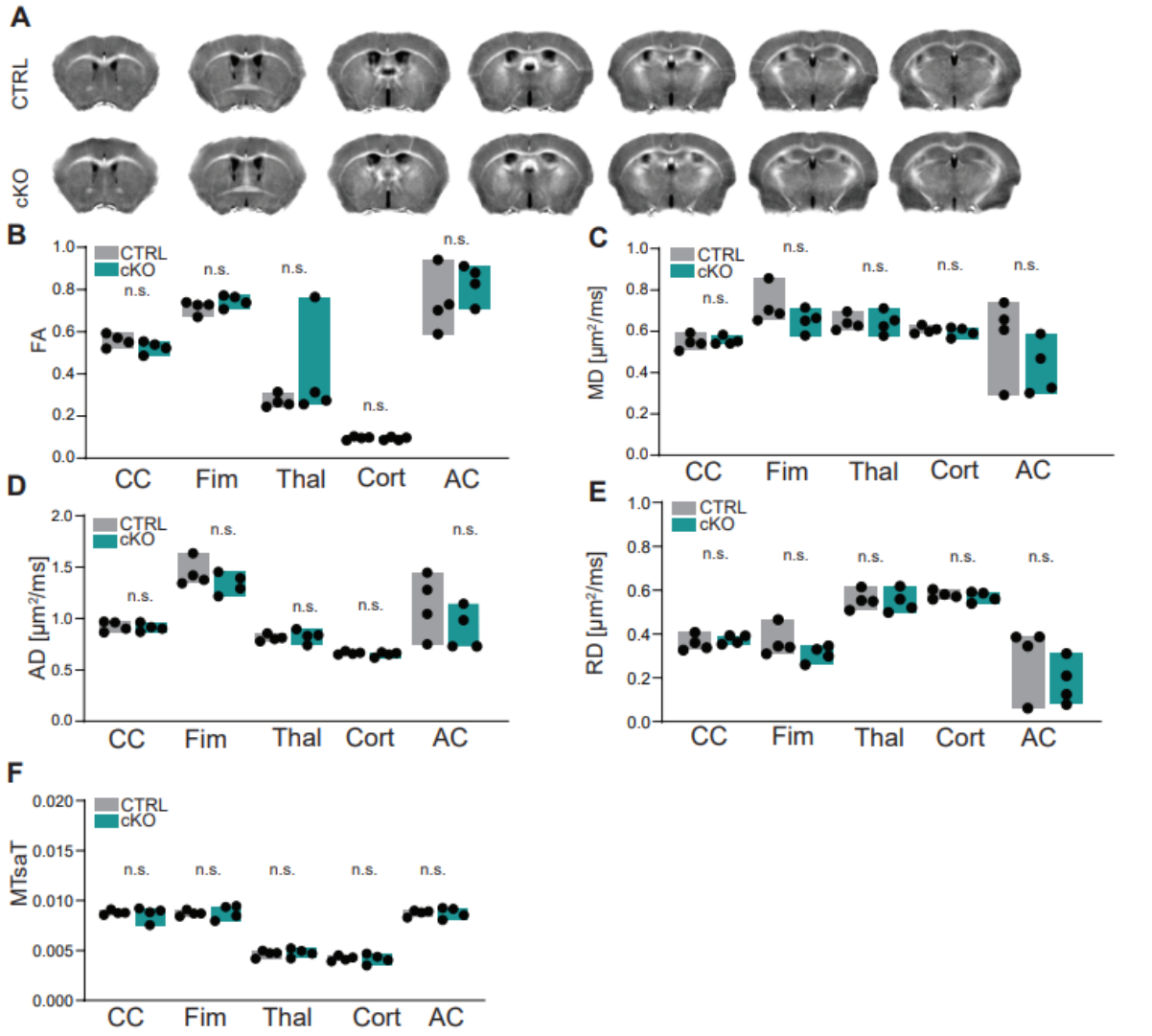

1433

1434

Buscham et al., Figure 3

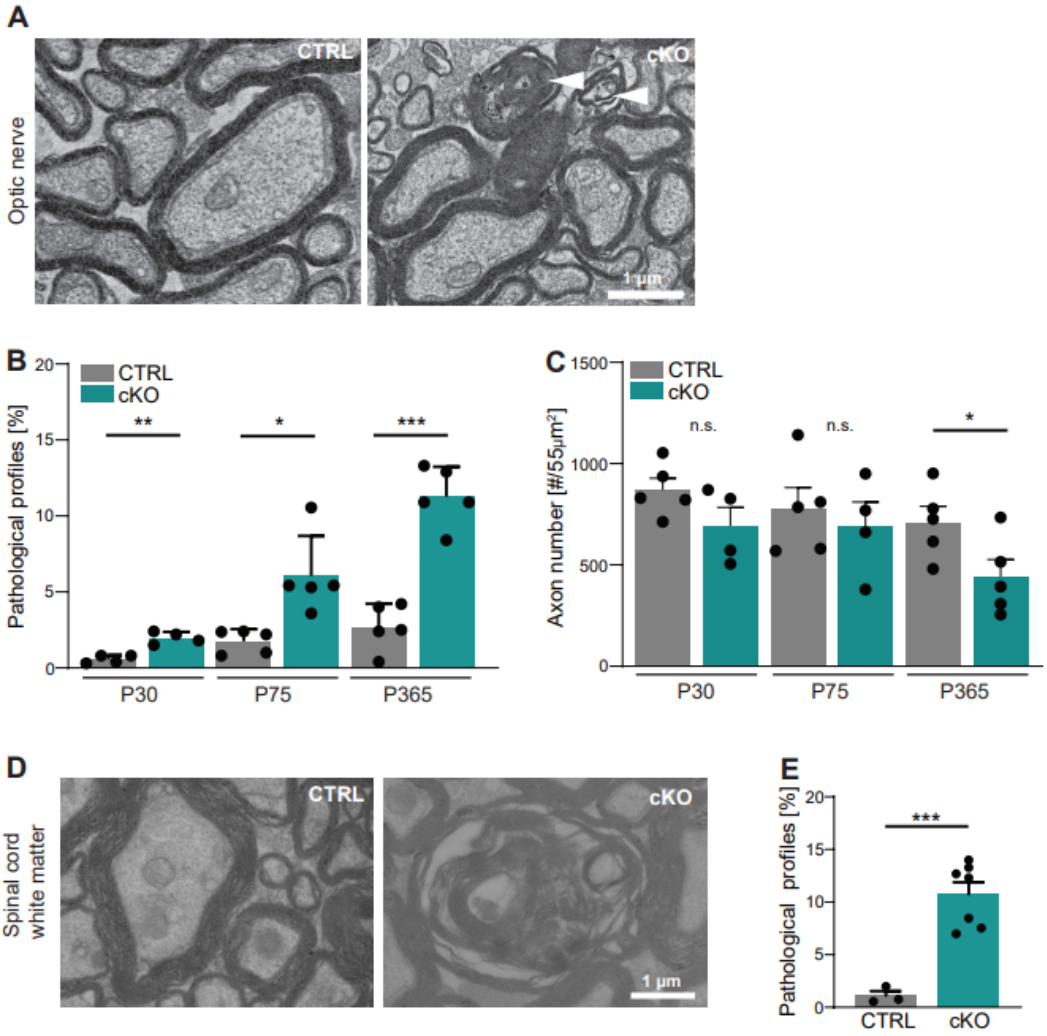

1435

1436

Buscham et al., Figure 3 Supplement 1

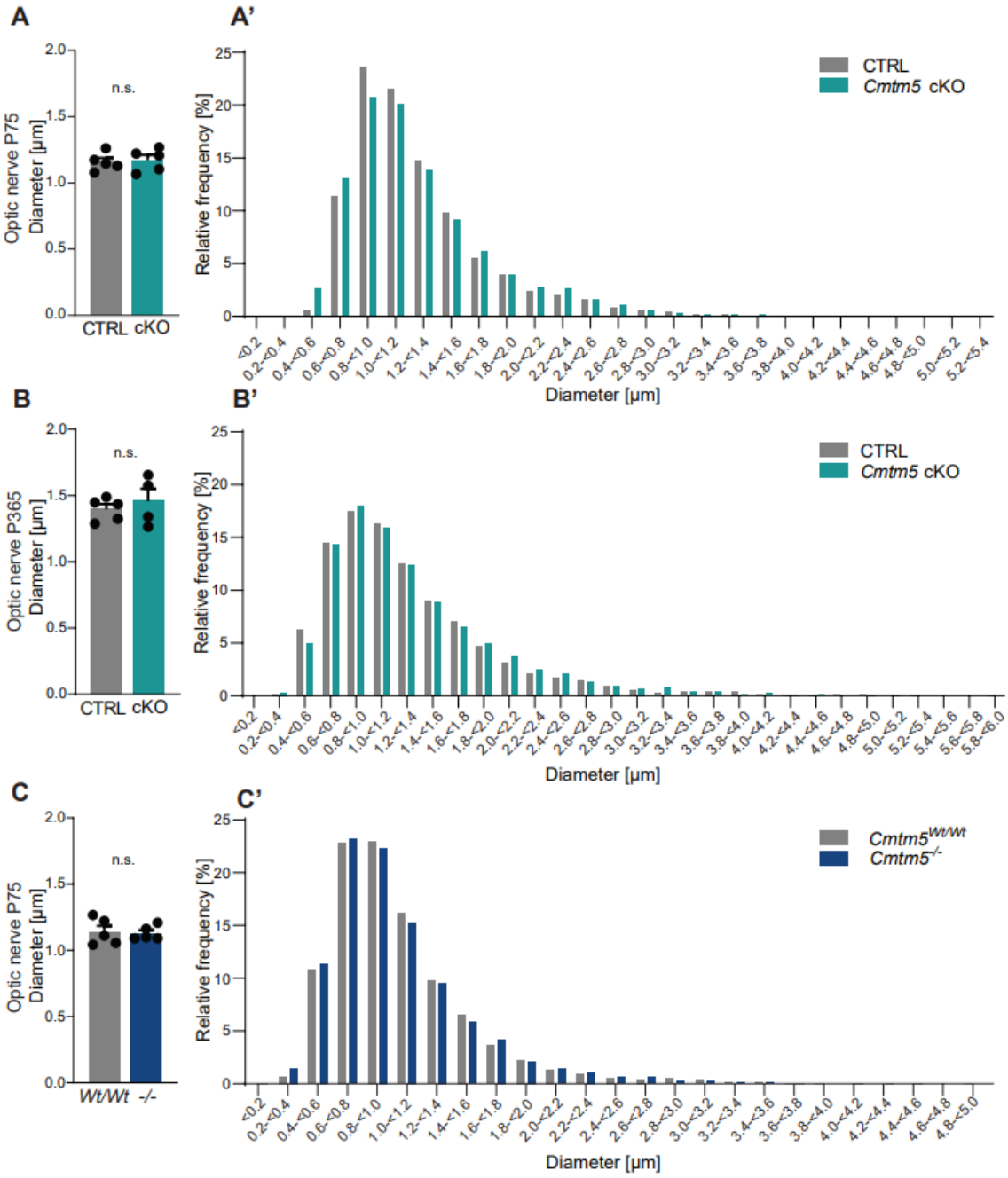

1437

1438

Buscham et al., Figure 3 Supplement 2

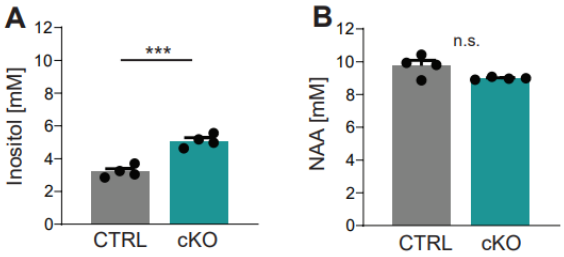

Buscham et al., Figure 3 Supplement 3

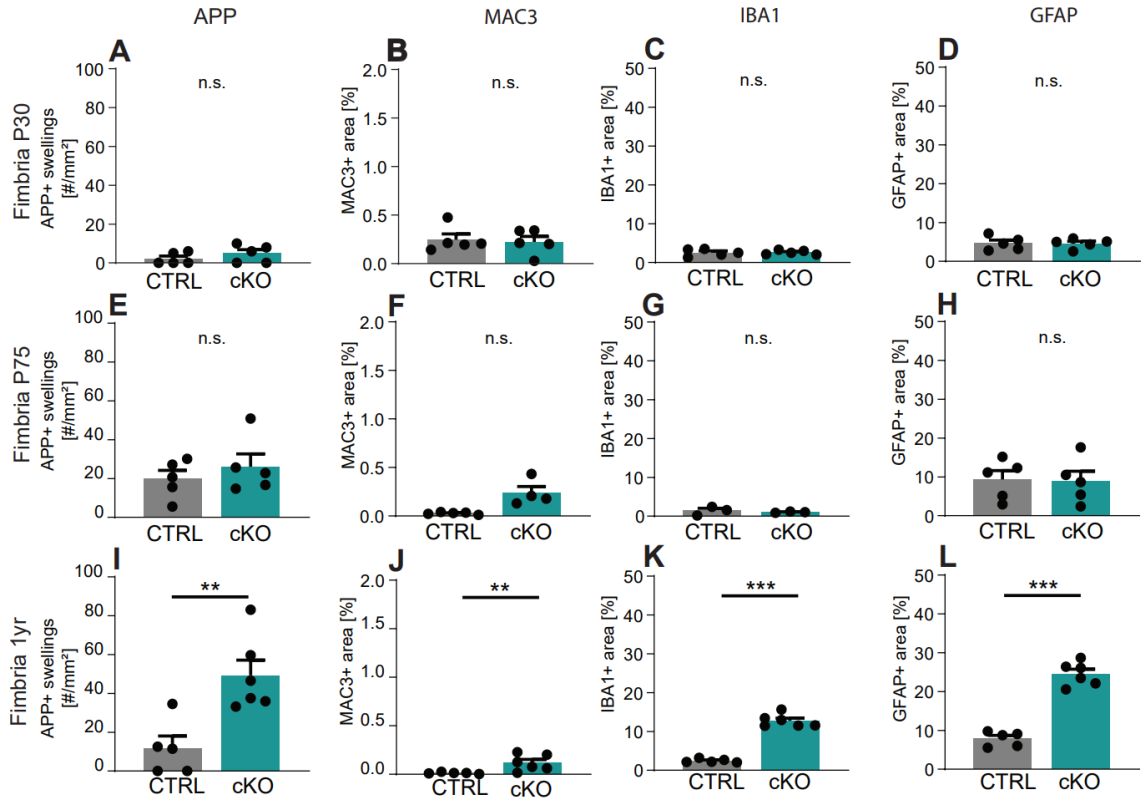

Buscham et al., Figure 4

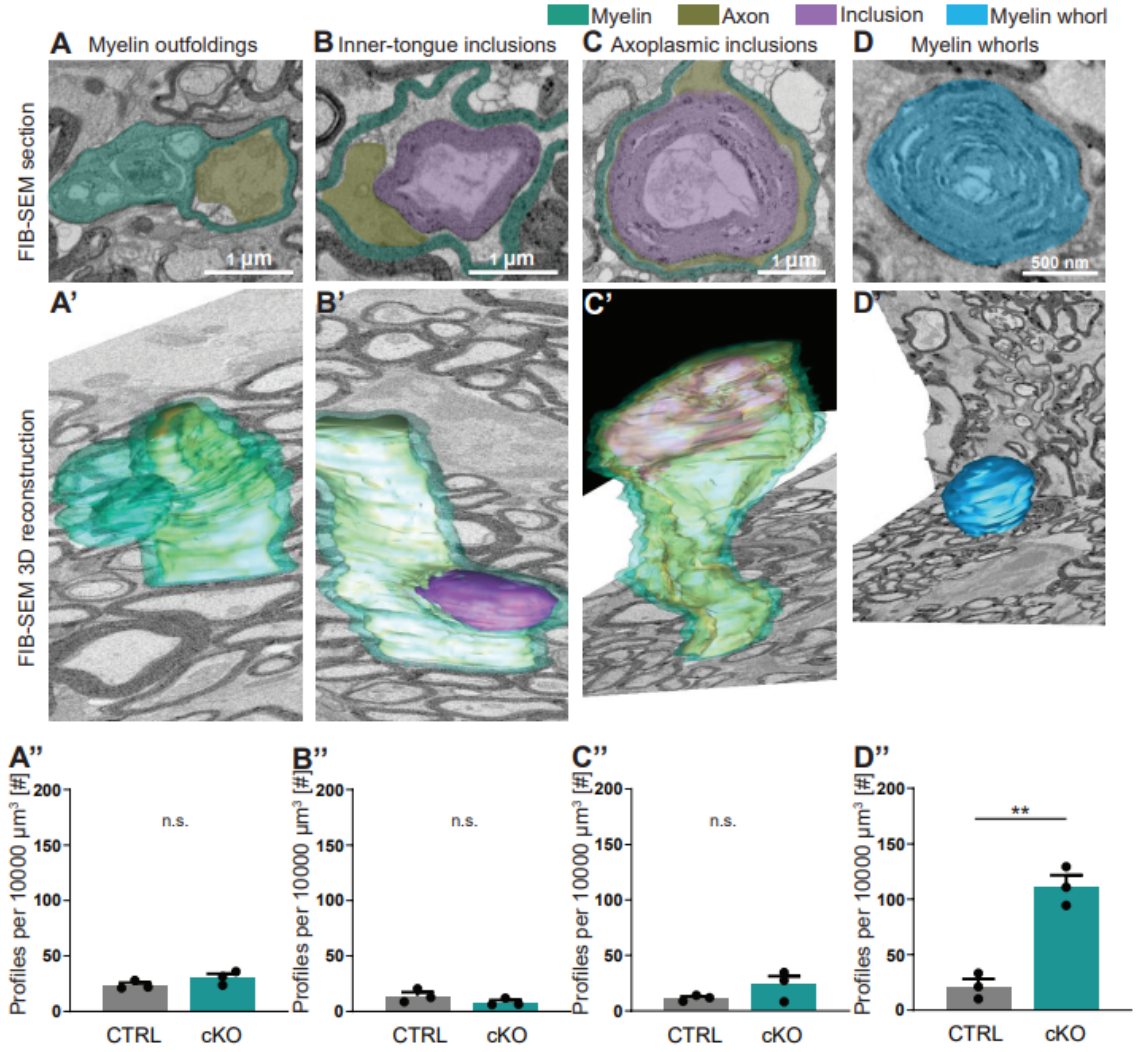

Buscham et al., Figure 5

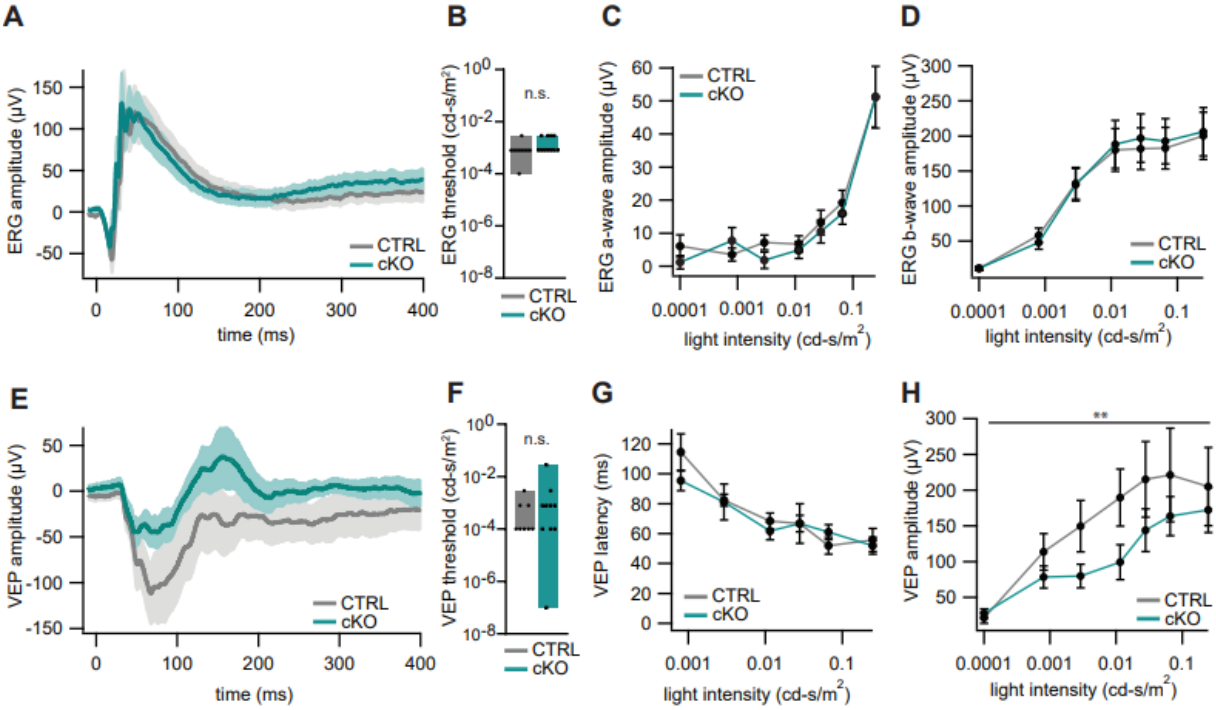

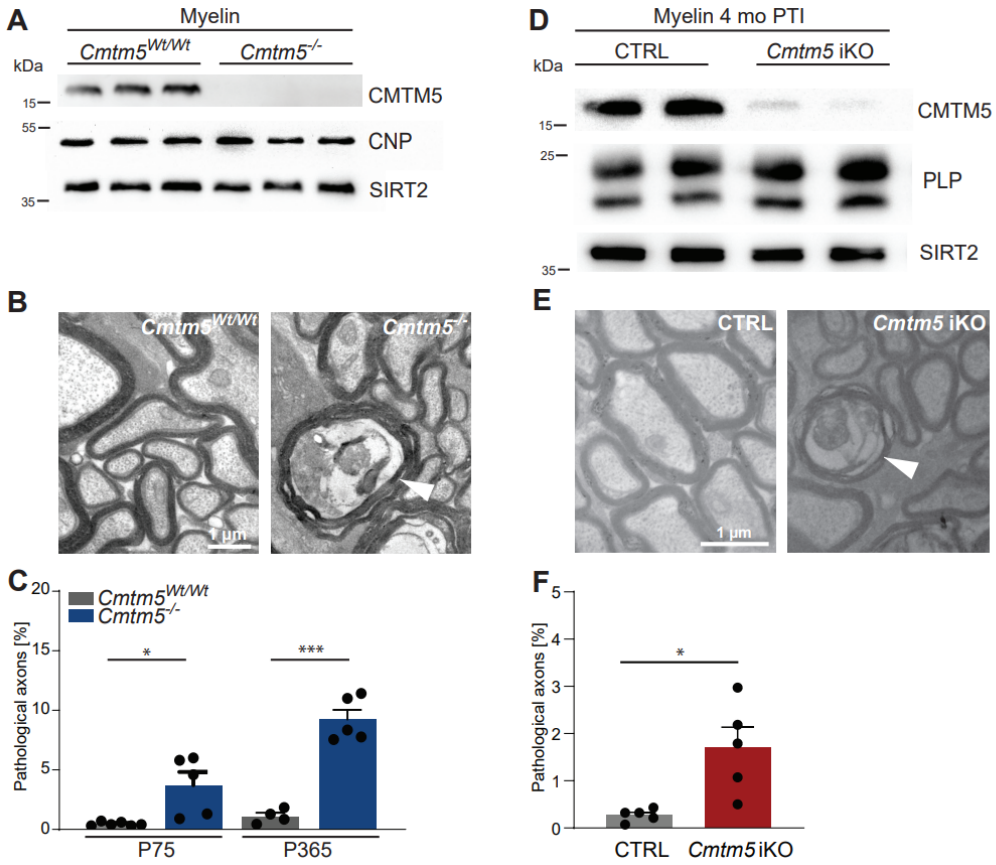

1447

1448

Buscham et al., Figure 6 Supplement 1

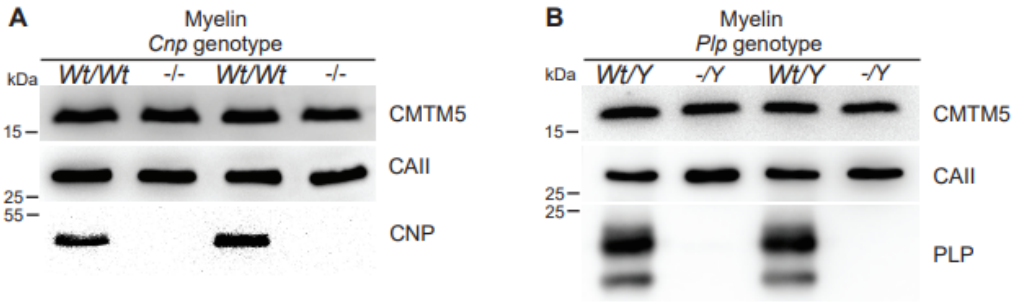

1449

1450

Buscham et al., Figure 7

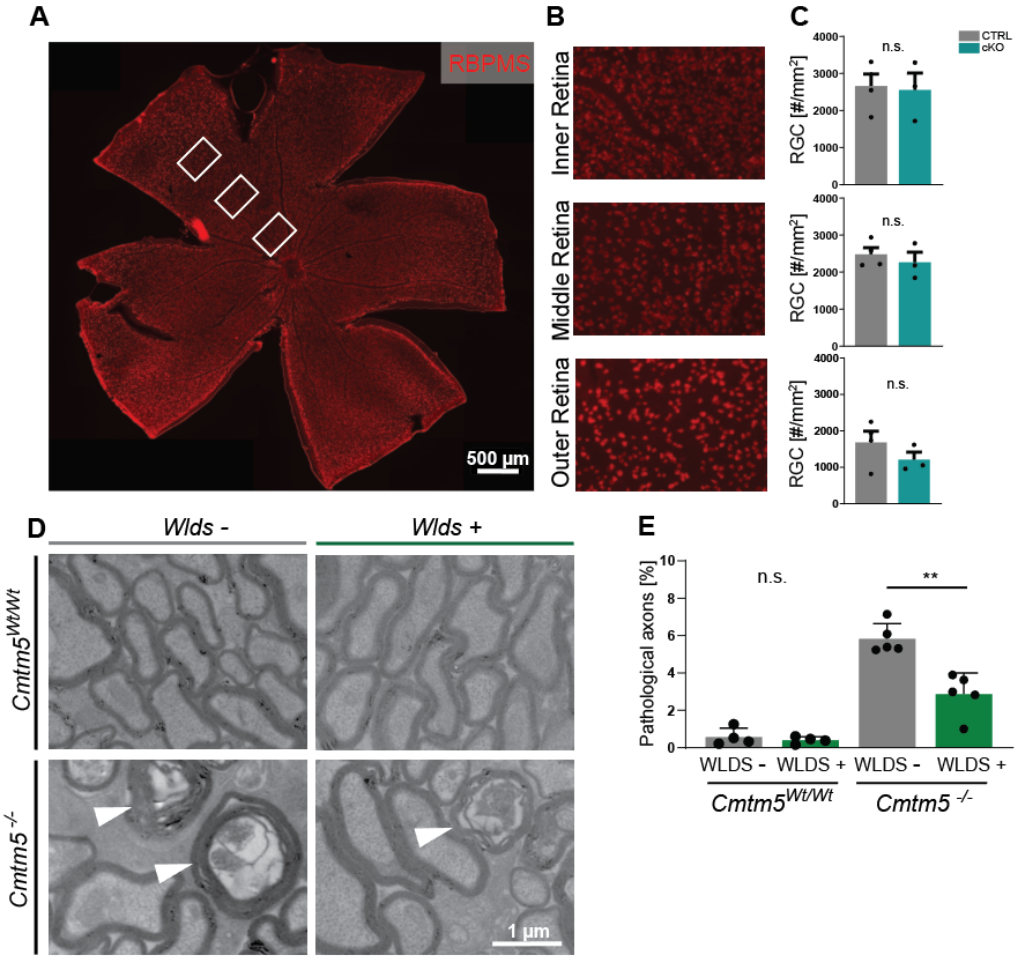

1451